Tribocorrosion behaviour of tin bronze CuSn12 under a sliding motion in NaCl containing environment: contact to inert vs. reactive counterbody

E. Huttunen-Saarivirta[1,*], L. Kilpi[1], A.T. Pasanen[1], T. Salminen[2], H. Ronkainen[1]

[1] *VTT Technical Research Centre of Finland Ltd, P.O. Box 1000, FI-02044 VTT, Finland*

[2] *Optoelectronics Research Centre, Tampere University of Technology, P.O. Box 692, FI-33101 Tampere, Finland*

*Corresponding author: Elina Huttunen-Saarivirta (elina.huttunen-saarivirta@vtt.fi).

Abstract

Tribocorrosion behaviour of tin bronze was examined in NaCl environments using two counterbodies: inert alumina and reactive bearing steel. The results with inert counterbody disclosed growing alloy losses with increasing potential, due to wear-influenced corrosion. Degradation progressed through the development, modification and removal of corrosion products, exposing fresh surface for the environment. With reactive counterbody, galvanic coupling between the two metals played an important role in the behaviour of the tribopair. At the lowest potential, where counterbody corrosion progressed slowly, the metals were in a direct mechanical contact, introducing wear in the ploughing mode in tin bronze. At anodic potentials, counterbody provided cathodic protection to tin bronze, with most material losses occurring in the counterbody by corrosion and wear-influenced corrosion.

Keywords: Tribocorrosion, corrosion, wear, galvanic coupling.

1. Introduction

First indications of copper alloys in the use of humankind date back thousands of years. Alloyed with tin, bronze enabled the manufacture of, e.g., weapons, tools, vessels and vases [1]. Today, tin bronzes of varying compositions are used in bearings, gears, piston rings, valves and fittings due to their high wear resistance, low friction coefficient against steel and favourable corrosion behaviour [2]. The alloy versions involving lead, called leaded tin bronzes, find use especially under conditions of water lubrication and where liquid lubricants cannot be applied at all, because soft lead provides solid lubrication [3] and the oxidized lead compounds further enhance the lubricative effect [4]. However, EU legislation aims at restricting the use of lead in bronze alloys at the concentrations above 0.3%. This has created a need for a detailed understanding of the behaviour of lead-free tin bronzes under various conditions.

Good bearing design involves three fundamental elements: knowledge of the service environment and how the material behaves there, plan and implementation of proper lubrication and selection of the best bearing material for the purpose [2]. Already this description implies that corrosion, i.e., metal-environment interactions, and tribology, i.e., wear, friction and lubrication related to the materials mechanical environment: surfaces in contact and relative motion, are closely linked with the application –and to each other, enabling tribocorrosion when occurring simultaneously. Indeed, tribocorrosion is a complex materials degradation process due to tribological contacts that occur in a corrosive environment, causing materials losses by the combined action of wear and corrosion, and changes in the friction coefficient. Because of the interaction between corrosion and tribology, the material loss rates due to tribocorrosion may be totally different from those predicted by the sum rate of the individual processes. [5-12]

In the case of tin bronze, one of the application environments is seawater [13] although some other copper alloys are more commonly used in seawater systems. It is known that the corrosion resistance of tin bronze relies on the patina layer, i.e., the corrosion products that develop on the alloy surface [14-17]. In NaCl containing environments, the selection of patina compounds is very

much potential dependent: under open circuit potential (OCP) conditions, both Cu_2O and SnO_2 evolve on the alloy surfaces [18,19], while under anodic potentials, the main species in the patina layer is CuCl [20,21]. Interestingly, CuCl is known to be a solid lubricant [22]. As for the tribological behaviour, friction coefficients ranging from about 0.6 to 0.8 have been reported for tin bronze-steel contacts [23,24]. The microstructure of the alloy has been demonstrated to be of great importance for the wear resistance [24], and the alloy is revealed to undergo work hardening to a significant extent under tribological contacts [23]. Nevertheless, the understanding of how corrosion and tribology interact, or do they actually interact, in the case of tin bonzes is completely lacking. Examples of other copper alloys, such as nickel aluminium bronze [25] and leaded tin bronze [26], enable to expect synergy between the processes, but the topic clearly requires further examination.

In this work, we aim to bridge some of the gaps in the current understanding of tribocorrosion behaviour of tin bronzes. The CuSn12 alloy is subjected to contact by two types of counterbodies: inert alumina and reactive bearing steel, in a relative sliding motion and under a constant load in a NaCl containing environment; such approach provides fundamental understanding of the behaviour of the alloy in ideal and real tribosystems. In the case of the ideal tribopair involving the inert alumina counterbody, the main questions to be answered are whether the corrosion products that evolve on the surfaces of CuSn12 alloy provide solid lubrication and if some other type of synergy is observed when mechanical contact and corrosion influence materials performance simultaneously. Thus fundamental mechanistic information about the materials tribocorrosion behaviour is obtained. In the real tribopair with the bearing steel as the counterbody, relevant information concerning many industrial tribosystem is collected, particularly when compared to the ideal case. The results are unique and may be exploited in the development path towards lead-free bearing solutions and operational optimization of the tribocorrosion systems.

2. Experimental

2.1. Materials

Tin bronze CuSn12 was the test material of this work. The alloy was obtained as cast ingots of the diameter of 42 mm, from which the disc specimens of the diameter of 40 mm and the thickness of 6 mm were machined. The disc surfaces were ground, subjected to lapping and finally polished down to 1 μm surface finish that introduced the surface roughness of 0.69 μm (R_a). Before the tribocorrosion tests, the disc specimens were cleaned in an ultrasonic bath first using acetone and then ethanol, both for 5 minutes.

2.2. Tribocorrosion tests

The alloy was subjected to tribocorrosion experiments using a Pin-on-Disc (PoD) Tribometer by Anton Paar Tritec. The POD device contained an electrochemical cell that was attached to the rotating shaft, as earlier described in, e.g., [26]. The disc specimens were located at the bottom of the cell and used as a working electrode (WE) in electrochemical measurements. The cell, the specimen holder, that enabled only the front surface of the disc specimens (10.6 cm^2) to be exposed to electrolyte, and the counterbody holder were made of polyether ether ketone (PEEK) polymer so that they did not contribute to the collected electrochemical data. The experiments were performed using two types of counterbodies. In the majority of experiments, the counterbody was an inert alumina ball (Al_2O_3, grade 5) of 10 mm in diameter and 0.03 μm of surface roughness (R_a). In these experiments, the normal loads of 1 and 5 N were applied through the level mechanism. The loads correspond to shear stresses of 117 and 200 MPa in the disc, of which the former is below and the latter well above the yield strength of the alloy ($R_{0.2}$ >130 MPa, typical Young's modulus around 100 GPa). The rotating speed of the shaft was controlled by computer and set to 100 rpm, yielding the linear sliding speed of 0.1 m s^{-1}. Some of the experiments were carried out using an electrochemically reactive bearing steel ball counterbody (100Cr6), with the diameter of 10 mm, exposed area of 0.3 cm^2 and the surface roughness lower than 0.01 μm. These tests were done

under the normal load of 5 N, introducing the shear stress of 176 MPa, and the linear sliding speed of 0.2 m s^{-1}. In all experiments, the diameter of the wear track was 20 mm. Friction coefficient was measured by the POD device during the tests employing mechanical load and recorded by computer.

During the tests, the contact occurred in the electrolyte: 30 ml of NaCl solution, which was contained in the electrochemical cell. Three NaCl concentrations were employed in the tests: 0.01 M, 0.6 M and 1.0 M, yet majority of the experiments were done in 0.01 M NaCl (inert conterbody) and 0.6 M NaCl (reactive counterbody). In each case, the electrolyte was prepared using ion-exchanged water and analytical-grade NaCl, with a fresh solution being used in each test. In the electrochemical measurements, the used reference electrode (RE) was a Ag/AgCl filled with 3.0 M KCl (0.21 V vs. standard hydrogen electrode, SHE) and it was positioned at the distance of 2 mm from the counterbody; all potentials presented here are given against a Ag/AgCl electrode. A ring of a platinum wire with the surface area of 6.0 cm^2 was used as a counter electrode (CE) and placed at the outer periphery of the cell. The electrochemical measurements were done in two ways: first by potentiodynamic polarization and then by potentiostatic measurements. The potentiodynamic polarization measurements were conducted after the stabilization period of 60 min, during which open circuit potential (OCP) values were recorded, at a sweep rate of 0.5 mV s^{-1} from -600 mV to 800 mV vs. OCP. The resulting polarization curves enabled the potential levels for potentiostatic measurements to be chosen. In the case of the inert counterbody, three potentials were selected for potentiostatic tests: one cathodic potential (-200 mV vs. Ag/AgCl) and two anodic potentials (100 and 500 mV vs. Ag/AgCl). In the case of the reactive counterbody, four potentials were selected: one cathodic potential that was below OCP of tin bronze (-400 mV vs. Ag/AgCl) and three anodic potentials (-275, -150 and -50 mV vs. Ag/AgCl). Table 1 summarizes the test conditions, which were employed in the experiments. Potentiostatic tests were conducted for the duration of 2 h (7200 s). All electrochemical measurements were performed with a Gamry Reference 600™ potentiostat/galvanostat/zero resistance ammeter and a Gamry Framework software. Furthermore, all experiments were carried out separately using fresh specimens, at the controlled temperature of 22±1 °C and humidity of 50±5 % RH. Two parallel experiments were performed under each set of conditions, each with fresh specimens and electrolyte.

2.3. Characterisation

The ground and polished as well as further etched specimens were examined under an optical microscope Leica MEF 4M and photographed using an attached DFC 450 camera. X-ray diffraction (XRD) measurements using a PANalytical X'Pert Powder facility and CuKα radiation (40 mA, 45 kV) through 10-120° range in 2θ scale were conducted in order to define the phases included in the alloy. The scan step was 0.013° and the scan rate 0.055° s^{-1}. The elemental compositions of the phases were determined using a Noran energy-dispersive spectrometer (EDS) system attached to a Zeiss ULTRAplus field emission scanning electron microscope (FESEM). Hardness of the alloy was determined using a Vickers indenter, a load of 1 kg, i.e., 9.81 N, a DuraScan20 facility and five repetitive measurements.

One of the two parallel specimens from potentiostatic tests were subjected to a thorough characterisation. After the tests involving the mechanical load applied on the inert counterbody, the alumina ball and the wear track were studied using an Olympus BH2 optical microscope with a Leica DFC320 camera. The morphology and composition of corrosion products (tests without the mechanical load) and the details of the wear tracks (tests with the mechanical load) were investigated using a Zeiss ULTRAplus FESEM and the attached Noran EDS. The corrosion products that developed on the alloy surfaces in the absence of mechanical load were identified using XRD investigations, whereas those included in the wear tracks caused by the inert counterbody were characterized using Raman spectroscopy. The Raman spectra were measured using a Thermo Scientific DXR2xi Raman spectrometer. The excitation laser wavelength was 455 nm and the laser power was 0.3 mW to avoid heating of the sample. Hardness values were determined from the wear track and, for comparison, from the top surface outside the wear track using an Ultra Nanoindentation Tester (UNHT) by Anton Paar Tritec, a Berkovich indenter (radius 50 nm) and a load of 1500 μN.

The volume losses by tribocorrosion were determined by measuring the cross-sectional wear track area in four locations (every 90° position) per sample using a Mitutoyo Formtracer SV-C3100 2D profilometer and multiplying the average value by the circumferential length of the wear track (πx20 mm). Under the combined action of wear and corrosion, the total material losses, *T*, in the wear track form by adding up the contributions by pure mechanical wear (*W*), active dissolution by pure corrosion (*C*) and the interaction between the two degradation processes, called synergy (*S*), following [25, 27,28]:

$T = W + C + S$ (Equation 1)

T is here determined experimentally based on the defined cross-sectional area of the wear track times the circumferential length of the wear track (2πx10 mm), Fig. 11b. The contribution by wear in the material losses in the disc specimens may be defined following the ASTM standard procedures [29, 30]:

$$W = 2\pi R\left[r^2 sin^{-1}\left(\frac{w}{2r}\right) - \left(\frac{w}{4}\right)\sqrt{4r^2 - w^2}\right]$$ (Equation 2)

where *R* is the sliding radius ($\frac{d}{2}$), *w* is the average width of the wear track (defined based on the wear track cross sections, Fig. 11a), and *r* is the radius of the counter body ball (5 mm). In the case of pure wear, the wear track width is defined from the experiments done at the cathodic potential. Furthermore, the wear-corrosion synergy may be twofold: on one hand, mechanical wear may influence corrosion (ΔC_W) and, on the other hand, corrosion may contribute to mechanical wear (ΔW_C), giving:

$S = \Delta C_W + \Delta W_C$ (Equation 3)

The term ΔW_C, called corrosion-influenced wear, may be calculated by:

$\Delta W_C = W_C - W$ (Equation 4)

where *Wc* is the wear volume in the presence of corrosion and *W* is the wear volume in the absence of corrosion as defined using Equation 1). Also W_C may be obtained using Equation 1, but wear track width values are defined at the anodic potentials. Then, the contribution by the other synergy component, ΔC_W, termed wear-influenced corrosion, may be defined as:

$\Delta C_W = T\text{-}W\text{-}\Delta W_C$ (Equation 5)

as the contribution by pure corrosion in the wear track is negligible; this is justified by the simultaneous of action of wear, thus within the wear track all corrosion is influenced by tribology. In the case of experiments with the reactive counterbody, the specimens were weighed before and after the tests to the precision of 0.01 mg. After all experiments, the morphology and composition of corrosion products (tests without the mechanical load) and the details of the wear tracks (tests with the mechanical load) and the counterbody surfaces were investigated using a Zeiss ULTRAplus FESEM and the attached Noran EDS. Additionally, the electrolytes used in the experiments were analyzed with respect to their Cu and Fe contents using inductively coupled plasma optical emission spectroscopy (ICP-OES) technique according to the ISO 11885 standard. The presented values are the average of two samples.

3. Results and discussion

3.1. As-received material

Optical micrographs of the material microstructure are shown in Fig. 1. The alloy had a two-phase structure containing a matrix phase, seen in light brown contrast in optical micrographs, and elongated islands of a minor phase, typically of 10-50 μm in length, seen in light grey contrast in optical micrographs. EDS analyses revealed the matrix phase to be clearly Cu-rich, containing on average 9.3 wt.% Sn, while the minor phase contained somewhat more Sn, on average 22.8 wt.%. Based on the Cu-Sn phase diagram and literature, these are the α-Cu and δ-$Cu_{41}Sn_{11}$ phases [31,32]. Much of the minor phase was located in the inter-dendritic areas of the cast microstructure, yet areas of it could also be detected within the dendrites. XRD investigations confirmed the presence of two phases (Fig. 2a): the major phase, the peaks of which corresponded well to $Cu_{0.9}Sn_{0.1}$ and with slightly shifted peak locations as compared to Cu, and the minor $Cu_{41}Sn_{11}$ phase. Hardness of the alloy, HV_1, was 124 with the statistical standard deviation (σ) of 9.

3.2. Tribocorrosion tests with the inert counterbody

In order to respond to the question if the corrosion products that evolve on the surfaces of CuSn12 alloy provide solid lubrication, the selection of test parameters aimed at as low friction coefficient as possible. Therefore, experiments were started using various test conditions, i.e., concentration of the NaCl solution and applied load, in order to define their roles in the behaviour of the alloy. The conditions that were most potential to yield a low friction coefficient were then chosen for the examination of the tribocorrosion behaviour in the presence of the inert counterbody.

3.2.1. Test conditions

Fig. 3 shows the influence of test conditions on the behaviour of tin bronze in the absence of the load (pure corrosion) and under the applied load of 5 N (tribocorrosion, inert alumina counterbody) at two NaCl concentrations: 1.0 M and 0.01 M. At both concentrations, the applied load slightly lowered the open circuit potential (OCP) of the alloy in the beginning of the test, whereas the progress in sliding equalized the potential differences (Fig. 3a). The higher NaCl concentration, 1.0 M, gave rise to a more active behaviour than the concentration of 0.01 M, because the OCP was shifted about 150 mV to the negative direction. This implies a greater driving force for corrosion at the higher concentration. In polarisation curves (Fig. 3b), higher current densities under anodic potentials by roughly one order of magnitude were evident at the concentration of 1.0 M than at the lower one. This demonstrates that, besides thermodynamics, also kinetics of corrosion were modified by the electrolyte concentration. At the higher concentration, the mechanical load of 5 N shifted the anodic current density values towards slightly higher values as compared to corresponding situation without the applied load, while at the lower concentration, the opposite was true. The evolution of friction coefficient during the OCP and polarisation measurements that were run in a row (Fig. 3c) disclosed overall lower values at the lower concentration, i.e., in 0.01 M NaCl. At both concentrations, the friction coefficient increased continuously during the OCP stabilization stage, from the initial value of about 0.2 up to 0.45 (0.01 M NaCl) or to 0.5 (1.0 M NaCl), then decreased slightly during the cathodic part of the polarisation curve and showed divaricate trends at the anodic branch of the polarisation curve: first reached the minimum at small anodic overpotentials and finally raised to the maximum values with increase in polarisation. Based on

these observations, the lower concentration, 0.01 M, was considered a more feasible with respect to the goal of low friction coefficient.

Fig. 4a shows the development of OCP during the stabilization period using the loads of 5 N and 1 N as compared to pure corrosion case (no applied load) at the NaCl concentration of 0.01 M. The mechanical load of 1 N did not influence the OCP level of the alloy significantly. At 5 N, the negative potential shift as compared to pure corrosion case was retained all through the study period, being most prominent at the beginning of the test. Overall, the results suggested the OCP level of the alloy decreased with increase in the applied load, consistent with literature [5,33]. The applied load influenced also the polarisation curves (Fig. 4b). As compared to pure corrosion case (no load), the use of load of 1 N slightly shifted the cathodic and anodic branches of the polarisation curve towards higher current density values, implying, e.g., slightly higher corrosion rate. The load of 5 N did not clearly contribute to the cathodic section but introduced a decrease in anodic current density values as compared to situation without the applied load. These results indicate that that the mechanical load of 5 N is beneficial for the corrosion resistance of the material and requires further analysis. The development of friction coefficient during the tests is shown in Fig. 4c. At the load of 1 N, the scatter in friction coefficient values was significant during the OCP phase of the measurement, and the values were also higher than at 5 N, with the maximum value reaching almost 0.55. Upon shifting to potentiodynamic polarization measurements, friction coefficient decreased to 0.35 (5 N) and even lower (0.25, 1 N), but with increase in potential, friction coefficient featured the same two-phase behaviour of low values at small anodic overpotentials and then clearly higher values with increase in polarisation. The low-friction-coefficient region was at around 100 mV above the OCP, with friction coefficient as low as 0.1 being detected at the load of 5 N.

The behaviour of tin bronze in the NaCl environment was dominated by active dissolution. Under all test conditions, the active dissolution slightly intensified with increase in polarisation, implying the system was sensitive to slight changes in solution oxidation capacity. The active dissolution was particularly pronounced in 1.0 M NaCl solution, due to greater corrosion rate and Tafel-like

logarithmic dependency of current density values on the changes in potential. Under anodic conditions, corrosion products clearly formed on the specimen surfaces. In none of the cases was passivation observed, but in 1.0 M NaCl current density values above the potential of about 0 mV vs. Ag/AgCl increased at a much lower rate than at lower overpotentials, suggesting a protective character. The formation of corrosion products on the specimen surfaces also explains the negative shift in OCP by the sliding contact, as corrosion products were then removed, exposing active metal in the wear track for further corrosion reactions. The influence of applied mechanical load on the polarization curves was much less pronounced than that of NaCl concentration. The detected minor decrease in anodic current densities at the load of 5 N in 0.01 M NaCl as compared to other studied test conditions may be explained by the modification of chemistry, by compound selection, or nature of the corrosion formed product layer. As for the friction coefficient, the moderate but increasing friction coefficient values during the OCP measurements probably relate to the removal of the natural oxide film and the gradual development of metal-ceramic contact. The noteworthy decrease in friction coefficient in the anodic region may be explained by, e.g., the development of a solid surface film that shows a lubricating effect. It has also been suggested [34] that metal ions that dissolve in the active region may act as lubricant; this is another possibility. The high final friction coefficient was typical of high anodic potentials and probably due to increase in the surface roughness with the propagation of corrosion [34]. Based on the obtained results, the NaCl concentration of 0.01 M, the applied load of 5 N and the three potentials marked in Fig. 4b, i.e., -200, 100 and 500 with respect to Ag/AgCl, were selected as the test conditions for further studies with the inert counterbody.

3.2.2. Tribocorrosion behaviour

Potentiostatic measurements were performed in order to understand the influence of applied potential on the behaviour of tin bronze, i.e., define the wear-corrosion synergy, and the selection and morphology of corrosion products that form on the alloy surfaces. At the lowest potential (Fig. 5a), cathodic current was recorded, thus no corrosion product formation was expected, consistent with the data from polarization curves. The situation corresponds to the case of pure wear (with the electrolyte acting as lubricant), as earlier in corresponding cases highlighted by, e.g., Sun and Rana

[28], Takadoum [35] and Chen et al. [36]; this was the aim here. At the potential of 100 mV vs. Ag/AgCl, the recorded current density values were systematically positive, implying that corrosion contributed to the materials behaviour (Fig. 5b). Nevertheless, no significant differences were detected in the overall current density levels. Up to the halfway of the test, the detected values were higher in those experiments that involved mechanical contact to the counterbody (tribocorrosion), but they stabilized towards the end, yielding, on average, equal current density levels irrespective of the test mode (corrosion vs. tribocorrosion). At the potential of 500 mV vs. Ag/AgCl, the current density values for tin bronze were heavily dependent on the test mode: in the case of corrosion, the current density values were more than one magnitude lower than those detected in the case of tribocorrosion (Fig. 5c). Indeed, in the absence of mechanical contact, the current density values peaked at the early stages of the test at $2x10^{-5}$ A/cm^2 but decreased to $4x10^{-6}$ A/cm^2 or lower towards the end of the test period. In the experiments involving the mechanical contact to the counterbody, the initial current density values of $5x10^{-3}$ A/cm^2 decreased during the first 30 min of the experiment, after which they stabilized to the level of $5x10^{-4}$ A/cm^2.

SEM studies revealed that, at the lowest potential, the surfaces were intact (Figs. 6a and b), as expected, and contained only minor amounts of oxygen besides the elements from the alloy (Table 2). Such low oxygen contents may result from post-test exposure to air, although the specimens were stored in a desiccator. The two-phase structure was also clearly resolved here, with consistent composition as reported above. XRD analyses (Fig. 2b) disclosed only the two phases that were present in the as-received material, consistent with SEM/EDS examinations. At the potential of 100 mV vs. Ag/AgCl, a layer of the corrosion products was observed on the alloy surfaces and it featured an irregular and heterogeneous morphology. Three types of areas were identified, indicated by numbers 3-5 in Fig. 6c-d and Table 2. The first type (indicated by number 3) included inner areas of the grains, covered by a relatively thin and uniform layer of corrosion products, with primarily oxygen and some (few wt.%) chlorine being detected by EDS analyses in addition to the elements from the alloy, at the ratio that corresponded to the major phase. Occasionally these areas contained some irregular and loose grains or nodules of corrosion products (with the relatively consistent composition with respect to the thinner sections) on the top. The second type (4) corresponded to the minor Sn-

rich phase oxidized, with also some chlorine being detected by EDS analyses. The third area type (5) was often located at the grain or phase boundaries and contained plenty of chlorine, yet some oxygen was also detected in EDS analyses. Particularly the latter type of areas were thicker than most of the surrounding areas, implying some thickness variation between local areas of the corrosion product. XRD investigations revealed the presence of Cu_2O and CuCl in addition to the phases included in the alloy (Fig. 2c), thus the chlorine-rich areas were likely CuCl. At the highest potential, the layer of corrosion products was more uniform than at the lower potential (100 mV vs. Ag/AgCl) but somewhat layered in structure (Fig. 6e). The more uniform and compact morphology likely contributed to lower current density values than at the potential of 100 mV vs. Ag/AgCl (Figs. 5b and c). The outermost layer of the corrosion product was rich in oxygen, whereas the underlying layer contained also plenty of chlorine (Fig. 6f, Table 2) and separate nodular areas with high oxygen content. The results from XRD analyses revealed only Cu_2O in addition to the phases in the alloy, supporting the EDS characterization data concerning the dominance of oxygen-bearing compounds on the surface.

Optical micrographs of the wear tracks and the alumina counterbody surfaces are shown in Fig. 7. At the potential of -200 mV vs. Ag/AgCl, the width of the wear track was the narrowest among the studied cases, 270± 10 μm (Fig. 7a), which was one and half times the Hertzian contact radius of 160 μm. Wear in the ploughing mode was evident within the wear track. Examination of the counterbody surface revealed transfer of tin bronze from the disc (Fig. 7b), possibly as a result of some of the abraded disc material being agglomerated on the counterbody surface. At the middlemost potential, the width of the wear track in the tin bronze specimens was greater than at the lowest potential: 350 ± 10 μm (Fig. 7c). The counterbody contained material transferred from the disc specimen, probably abraded corrosion products as charged on the basis of the brownish colour and lack of metallic shine (Fig. 7d). At the potential of 500 mV vs. Ag/AgCl, the width of the wear track was too wide to be examined at full width by stereomicroscopy. Nevertheless, the investigation disclosed ploughing type of wear along with the presence of a bluish corrosion product layer (Fig. 7e). Also the counterbody surface reflected the greater width of the specimen-counterbody contact

than at the lower potentials plus the transfer of corrosion product from the disc to the counterbody surface (Fig. 7f).

SEM studies confirmed that, at the lowest potential, wear in a ploughing mode had occurred (Figs. 8a and b). The two-phase structure of the material could not be resolved within the wear track, but the surface featured oxidized grooves from the ploughing wear mechanism. Indeed, despite falling within the cathodic region, the wear track was clearly oxidized (Table 3), probably due to the creation of reactive fresh surfaces by the sliding contact and the presence of dissolved oxygen in the electrolyte. The Raman microscopy of the wear track confirms the presence of Cu_2O (Fig. 9a) [37-39]. At the potential of 100 mV vs. Ag/AgCl, the wear track was covered by a uniform corrosion product layer (Figs. 8c and d). The developed corrosion product was clearly more homogeneous with respect to microstructure and featured less thickness variation between individual spots as compared to the case without the mechanical load (Figs. 6c and d). Within the wear track, surface characteristics related to ploughing wear grooves could be occasionally resolved. Like at the lower potential, the two-phase microstructure was not identifiable in the corrosion product nor in the alloy underneath. Instead, relatively more porous and denser sections of the corrosion product could be observed. EDS analyses for the corrosion product revealed primarily oxygen and some chlorine (Table 3). The Raman spectrum collected from the wear track was equal to that at the lowest potential, confirming the presence of only Cu_2O (Fig. 9b). At the highest potential, SEM examinations showed the width of the wear track to be 640 ± 15 μm (Fig. 8e). The film morphology was levelled and compacted, yet also cracked (Fig. 8f). Compositionally, the corrosion product film contained plenty of oxygen, and the chlorine content was also high (Table 3). The wear track appeared least homogeneous under the Raman microscope, showing regions with different visual appearance, and the sample was the most sensitive to the laser damage. In addition to Cu_2O (Fig. 9c) some regions showed the OH-stretch vibrations around 3300 to 3500 cm^{-1} (not shown here). The presence of CuCl was not observed in any of the samples, although it could not be completely excluded as the peaks for crystalline CuCl would partially overlap with the Cu_2O peaks especially if the CuCl is defected.

The microscopic studies on the wear track in tin bronze revealed slight differences as compared to the pure corrosion case. At the cathodic potential of -200 mV vs. Ag/AgCl in the absence of load, only the phases present in the as-received material were detected. At the same potential in the presence of the inert counterbody and the load of 5 N, Cu_2O was observed along with the phases of the as-received alloy. This finding suggests that, due to the mechanical load, oxidation of the alloy is enhanced. At the anodic potential of 100 mV vs. Ag/AgCl, CuCl was included in the corrosion products in the case of pure corrosion, along with Cu_2O. Under the inert counterbody and the load of 5 N, only the presence of Cu_2O was confirmed. This observation indicates that the applied mechanical load influences the corrosion product phase selection, by inhibiting the development of CuCl. This may be because of the relatively slower kinetics of formation of CuCl than of Cu_2O between the contact situations of the counterbody or the local changes in surface conditions as compared to the corrosion cases. For example, Pyun and Chun [40] have reported that the formation of stable CuCl is often preceded by the transport of $CuCl_2^-$ ions to or the adsorbtion of metastable CuCl on the surfaces. At the highest potential, Cu_2O was the only compound detected irrespective whether the specimen was exposed to corrosion only or the combination of corrosion and mechanical load.

Friction coefficient records as a function of potential are shown in Fig. 10. At the cathodic potential, -200 mV vs. Ag/AgCl, friction coefficient was initially at a moderate level of about 0.4, but decreased to a value of about 0.2 by midway of the test. This was lowest friction coefficient value among the test conditions and retained until the end of the test period. At the potential of 100 mV vs. Ag/AgCl, the friction coefficient values showed a clear increasing trend with progress of the test, from the initial value of 0.2 to the final value of about 0.8. This was the highest friction coefficient level reached during the potentiostatic experiments, with possible explanations including increase in surface roughness due to the uneven spreading of the corrosion products on the wear track and the morphology of the developed corrosion products. At the highest potential of 500 mV vs. Ag/AgCl, friction coefficient values increased from the initial value of 0.2 to the peak of 0.65 during the first 1500 s, after which the values stabilised to the level of about 0.5. Such development may be

explained by the formation of corrosion products and their levelling (compaction, morphology flattening) under the contact to the counterbody.

Profilometer studies enabled wear track cross sections to be examined, Fig. 11a. At the potential of -200 mV vs. Ag/AgCl, the wear track was very shallow, with the maximum depth less than 2 μm. Due to the shallow nature of the wear track, the edges were not clearly resolvable but could mainly be detected based on the increased surface roughness as compared to the surroundings. Based on this methodology, the width was approximately 150 μm. At the potential of 100 mV vs. Ag/AgCl, the typical wear track depth was 6-7 μm and the width in the range from 310 to 340 μm, i.e., both much greater than at the lowest potential. At the highest potential, the wear track cross-section was clearly greater than at the lower potentials. The wear track depth reached almost 35 μm at maximum, while the width was about 600 μm. The cross-sectional profiles also revealed significant surface roughness outside of the wear track, likely due to the formed corrosion products. These results reflect the important role of potential in determining the extent of wear, due to the contribution by the corrosion process.

It has been earlier reported that tin bronze undergoes significant work hardening under tribological contacts [4]. Hardness values were determined within and outside of the wear track at the three potentials (Table 4). The results showed that, at the two lowest potentials, hardness values within the wear track were lower than in the areas surrounding the wear track. At the highest potential, the overall hardness values were clearly lower than at the two lower potentials and roughly equal independently of the area of interest, i.e., if measured within or outside of the wear track. At the lowest potential, the detected differences in the hardness values within and outside of the wear track may be explained primarily by the differences in surface flatness between the two measurement regions. However, at the potential of 100 mV vs. Ag/AgCl, the measured hardness values also reflect the greater thickness and porous nature of the corrosion product within the wear track, due to the great hardness decrease as compared to the cathodic potential. At the highest potential, the relatively low hardness values independently of the measuring area were probably due to corrosion product that covered the surfaces, thus the nanoindentation measurements only reached the

corrosion product. These results do not indicate any work hardening due to the great contribution of corrosion products to the materials surface behaviour. Nevertheless, the results suggest that the corrosion products that form on the alloy surfaces particularly at the highest potential are so soft that they are easily removed by the applied load.

3.2.3. Wear-corrosion synergy and tribocorrosion mechanism

The contribution by wear and the two synergy terms to the overall material losses are shown in Fig.11b. As described above, at the lowest potential, the conditions were cathodic, thus the contribution by corrosion was negligible, making mechanical wear the only degradation mechanism. The total material losses were very small, 0.03 mm^3. At 100 mV vs. Ag/AgCl, wear-influenced corrosion accounted for the majority (97%) of degradation, implying the corrosion product was relatively more easily removed than the tin bronze alloy, exposing fresh surface for further reaction. As the development of Cu_2O was the main surface process detected, these results mean that the formed product layer did not provide protection against wear, consistent with the much lower hardness as compared to the bulk alloy and the highest friction coefficient among the three potentials, and that the corrosion product layer was modified as compared to the case of pure corrosion. The total material losses were 2.1 mm^3, with the contributions by pure wear and corrosion-influenced wear being roughly equal (0.03-0.04 mm^3). At the highest potential, 500 mV vs. Ag/AgCl, material losses were almost entirely (99%) covered by wear-influenced corrosion. Furthermore, the extent of losses at the highest potential was much greater than at the two lower potentials, 27.1 mm^3, which means over tenfold material losses as compared to the middlemost potential. Mechanical wear significantly accelerated electrochemical corrosion, as may be seen in the current density records (Fig. 5c).

The obtained results show that the weak point of the alloy is potential dependent. At the lowest potential, where wear was the dominant degradation mechanism, the material losses were small. At the potential of 100 mV vs. Ag/AgCl, the electrochemical dissolution of the material played a key role. Due to the dissolution, corrosion products developed, being then easily removed by the

counterbody contact. At the highest potential, i.e., when mechanical load is applied simultaneously with high potential (oxidizing conditions), the main weakness was clearly wear-influenced corrosion. This was primarily related to the removal of the corrosion products and the following exposure of active fresh material to the environment. Thus the interactions between wear and corrosion were potential-dependent and the synergy significantly increased the material losses. This highlights the importance of characteristics of the corrosion product layer that develops on the alloy surfaces under various conditions. However, the ideal situation of solid lubrication was not reached at the potentials selected for potentiostatic tests, meaning a positive synergy between wear and corrosion was not observed, as indicated by the high absolute values of friction coefficient. This may be because the formation of CuCl in the presence of mechanical load was not detected, even if it was detected at 100 mV vs. Ag/AgCl in the absence of mechanical load. The likely explanation for this is the change in the conditions for ion transport and absorption at the tin bronze, so that they did not support the build-up of CuCl. Nevertheless, although the condition of solid lubrication was not achieved, we could definitely identify some interesting future research directions, such as the weak points of the alloy to be tackled by future alloy development.

3.4 Tribocorrosion tests with the reactive counterbody

In the tests using reactive bearing steel counterbody, the experimental conditions were chosen to promote the galvanic coupling between the electrodes (disc of tin bronze and ball counterbody of bearing steel). 0.6 M NaCl solutions was thus used as an electrolyte. Corresponding OCP and polarization measurements were conducted as in the case of inert counterbody. OCP records, Fig. 12a, revealed that bearing steel featured a significantly lower OCP (-520 mV vs. Ag/AgCl) than tin bronze (-150 mV vs. Ag/AgCl), thus bearing steel was cathodic to tin bronze and provided cathodic protection. As a result, the OCP measured during the tribocorrosion tests was actually a mixed potential of the galvanic couple, yet with the mechanical loading. The mixed OCP stabilized to the level of -350 mV vs. Ag/AgCl. These results demonstrate that the OCP values of tin bronze at the concentration of 0.6 M NaCl fell between those at the concentrations of 0.01 M and 1.0 M (Fig. 3a), consistent with expectations. In polarization curves related to pure corrosion conditions, Fig. 12b, it

could be seen that for both tin bronze and the bearing steel, logarithm of current density values grew almost linearly with increase in potential under anodic conditions, thus the materials experienced the dissolution of metal ions, with the current density values of bearing steel reaching at least one decade higher values than those of tin bronze. In tribocorrosion experiments with the bearing steel counterbody, the overall current density values of the tribosystem under anodic conditions were much lower than for either material alone because of the establishment of a mixed potential. This also indicates the galvanic coupling between the materials (with 1:35 surface ratio between anode and cathode) and cathodic protection of tin bronze by the bearing steel. Furthermore, the polarization curves enabled the potentials of interest for the potentiostatic experiments to be determined: -400 mV, -275 mV, -150 mV and 50 mV vs. Ag/AgCl. The first of the four potentials corresponds to cathodic situation of the tribopair, while the three latter potentials fall within anodic region of the curve.

As expected, the current density values at the lowest potential were systematically cathodic, implying no contribution from corrosion to materials degradation. At the potential of -275 mV vs. Ag/AgCl (Fig. 13a), the current density values for tin bronze under pure corrosion conditions were negative, thus no corrosion occurred in the alloy. However, when subjected to tribological contact by the bearing steel ball, the measured current density values were clearly positive. With increase in potential to -150 mV vs. Ag/AgCl (Fig. 13b), the same trends were detected than at the previous potential yet the overall current density levels were higher. With further increase in potential up to 50 mV vs. Ag/AgCl (Fig. 13c), the level of current density values still increased, yet the differences between pure corrosion and tribocorrosion cases diminished. There results revealed that the anodic current density values increased systematically with increase in potential and were higher than in the absence of the counterbody and mechanical load, referring to the increased corrosion rate in the materials.

SEM investigations of the tin bronze discs (Fig. 14) revealed wear in a ploughing mode in the wear track. At the three lowest potentials (Figs. 14a-f), plowing was the main wear mechanism, and the wear track contained corrosion products rich in oxygen and iron, clearly transferred from the

contacting bearing steel counterbody. At the highest potential (Figs. 14g-h), the wear track was clean from the corrosion product residues from the pin specimen. Instead, the wear track contained wear grooves, but the surrounding surface was covered by corrosion products rich in oxygen, copper and tin. SEM examinations of bearing steel pin specimens (Fig. 15) disclosed the development of oxygen- and iron-rich corrosion products on the steel surfaces at all studied potentials. At the three lowest potentials, corrosion products were mostly removed from the contact area but retained in the surrounding areas. Additionally, at the lowest potential, -400 mV vs. Ag/AgCl, transferred tin bronze was frequently detected in the contact zone (Figs. 15a-b). At the two middlemost potentials (-275 and -150 mV vs. Ag/AgCl; figs. 15c-f), the contact areas contained fewer corrosion products than the surrounding areas. These were removed by the mechanical contact to the disc specimens, by a plowing type of wear, as evidenced by the occasional deformation grooves detected in these areas (Figs. 15c-f). At the highest potential, -50 mV vs. Ag/AgCl, the pin specimen was completely covered by the oxygen-bearing corrosion product, with no bare deformed metal being detected at all (Figs. 15g-h).

Fig. 16 shows the evolution of friction coefficient during the 2 h experiments at each potential. At the lowest potential, -400 mV vs. Ag/AgCl, friction coefficient initially increased from the start value of 0.3 to the peak value of 0.5 within the first 2500 s, after which the values stabilized to the level of 0.4.The high values detected during the first third of the experiment may be related to the transfer of material between the metal surfaces, particularly from disc to pin, followed by a deformation and adjustment of the transfer layer to the mechanical contact during the stabilization period. At all other potentials, i.e., all anodic potentials, the friction coefficient values at the end of the experiment were higher than at the lowest potential and showed a steady yet slow increase all through the experiment. In all cases, the end-of-experiment friction coefficient values were around 0.5. It is likely that the corrosion products that developed on the surface of bearing steel counterbody specimens contributed to the increase in friction coefficient, given that these were few at the lowest potential and abundant at higher potentials. If compared to the tests conducted with the inert counterbody, friction coefficients recorded during the highest potential, 500 mV vs.

Ag/AgCl, were of the same order than those detected with the reactive counterbody at the anodic potentials.

Fig. 17a shows the wear track profiles of disc specimens from the experiments conducted with the reactive counterbody. The profile shape clearly varied between the four potentials. It was evident that material losses decreased with increase in potential, in contrast to experiments with inert counterbody. At the three lowest potentials, the profile was of U or V shape, yet the edge between the wear track and the surrounding areas was not as clear as in the case of inert counterbody. Opposite to these, at the highest potential, the wear track profile followed the shape of W, with two distinct minima being detected in the cross section. Additionally, the overall scatter in the profiles was high, demonstrating that the surfaces featured significant roughness. These two issues made the determination of wear track width extremely difficult, thus the degradation mechanisms could not be approached in the same way than in the case of inert counterbody experiments. Therefore, specimen weight loss measurements and electrolyte chemical analyses were conducted.

The results from weight loss measurements (Fig. 17b) revealed that in the case of pure corrosion, weight losses in the tin bronze disc specimens only realized at the two highest potentials, consistent with expectations from current density records (Fig. 13). In tribocorrosion experiments with the reactive counterbody, the situation changed completely. The highest weight losses in disc specimens were true at the lowest potential; these were even higher than in at the highest potential in the case of pure corrosion. At all other potentials, weight losses in disc specimens under the tribocorrosion conditions were much smaller than at the lowest potential. However, they slightly increased with increase in potential, reaching at 50 mV vs. Ag/AgCl the level of one tenth of material losses at the lowest potential. The weight losses in the pin specimens in the tribocorrosion experiments systematically increased with increase in potential. In evaluating these results, one must be aware that weight losses were actually a sum of weight losses by wear and active dissolution and weight gains by the development of corrosion products. Therefore, electrolyte analyses with respect to dissolved Cu and Fe contents shedded some more light on the topic. Indeed, electrolyte analyses (Fig. 17c) disclosed that in the case of tin bronze corrosion, Cu

concentration of the electrolyte was increased only at the two highest potentials, consistent with weight loss results. In the case of tribocorrosion experiments with a reactive bearing steel counterbody and the load of 5 N, detectable Cu contents of the electrolyte were evidenced at the lowest and highest potentials, whereas Fe contents of the electrolyte increased systematically with increase in potential. The electrolyte Cu content at the lowest potential was relatively much lower than the detected weight losses (Fig. 17b), referring to the significant contribution by wear to the overall weight losses. Indeed, as shown by SEM studies (Figs. 14 and 15), plowing wear mode of the tin bronze was observed under these conditions, together with transfer of worn material to the pin surfaces. In turn, the Fe contents in the electrolyte followed a consistent trend with the weight loss measurements.

Concerning the overall material loss mechanisms in the experiments with reactive bearing steel counterbody, there were clear differences to the tests conducted with inert counterbody, as the synergy terms could not be defined and the galvanic coupling between the disc and the pin dominated the surface processes. At the lowest potential, -400 mV vs. Ag/AgCl, wear through plowing was the primary damage mode for the tin bronze, enabled by a direct metal-metal contact. At the middlemost potentials, -275 and -150 mV vs. Ag/AgCl, corrosion of the bearing steel pin was the main degradation mechanism within the tribopair, providing cathodic protection via acting as a “sacrificial anode” to tin bronze. Wear of the surfaces also occurred but to a much smaller extent than at -400 mV vs. Ag/AgCl. At the highest potential, both the disc and the pin underwent anodic dissolution enabling corrosion products to be developed on the surfaces. These were mostly removed from the wear track of the disc but retained on the pin surfaces. It is likely that the corrosion products on the contacting surfaces contributed to the slightly higher value of friction coefficient than at the lower potentials.

4. Conclusions

The results presented in this paper enable the following conclusions to be drawn:

1) Corrosion of tin bronze in NaCl environments is dominated by active dissolution of the alloy and the related corrosion product development.

2) In the experiments involving the inert alumina counterbody, the contribution of corrosion to the degradation of tin bronze CuSn12 under cathodic conditions is negligible, thus the behaviour is pure wear. However, the material losses in the alloy remain low. Under anodic conditions, wear-influenced corrosion is the primary interaction term between wear and corrosion and the main failure mechanism of the alloy, with its contribution to the overall material losses growing significantly with increase in potential.

3) The corrosion product layer that forms on CuSn12 in 0.01 M NaCl is structurally and compositionally heterogeneous. As compared to the case of pure corrosion, mechanical load applied to the inert alumina counterbody influences the corrosion product layer morphology, by levelling and compacting the structure, and the compound selection, by introducing the Cu_2O already at the cathodic potential and inhibiting the formation of CuCl phase at anodic potential of 100 mV vs. Ag/AgCl. The latter is likely due to the modification of the conditions at the alloy surface, e.g., ion transport. Furthermore, the corrosion product is soft, being relatively more easily removed by the counterbody contact than the alloy itself.

4) In the experiments involving the reactive bearing steel counterbody, behaviour of the system is governed by the extent of bearing steel corrosion. At the lowest potential, where the extent of corrosion in the bearing steel is low, metal-metal tribological contact is of great significance for the material losses, with wear of the tin bronze disc being the main degradation mode. Wear losses against bearing steel are much greater than against alumina counterbody. With increase in potential to anodic values: -275, -150 and -50 mV vs. Ag/AgCl, the corrosion of bearing steel starts to dominate the behaviour, as it provides cathodic protection to the tin bronze. At the highest potential also corrosion of tin bronze influences the behaviour of the tribopair, with the highest friction coefficient being recorded due to contact between rough corrosion product layers on the surfaces.

5) The results show that the counterbody material has a significant influence on the behaviour of the tribopair. Although the inherent tribocorrosion behaviour of the alloy can only be assessed using an inert counterbody, the performance under the contact to the reactive counterbody should also be checked in order to avoid surprises in the use phase because the counterbody material influences both the electrochemistry and the Hertzian contact conditions.

Acknowledgements

The financial support for the SUBTRIB project from the Finnish Funding Agency for Technology and Innovation (earlier: Tekes; decision number 865/31/2016), participating companies and VTT Technical Research Centre of Finland Ltd is gratefully acknowledged. Mr. Simo Varjus is thanked for conducting the pin-on-disc experiments.

References

1. R. Francis, Corrosion of Copper and its Alloys - A Practical Guide for Engineers. NACE International, Houston, USA, 2010.

2. www.copper.org (viewed on 08.01.2020).

3. G.W. Stachowiak, A.W. Batchelor, Engineering Tribology (4rd Edition). Elsevier, Oxford, UK, 2014.

4. S. Equey, A. Houriet, S. Mischler, Wear and frictional mechanisms of copper-based bearing alloys. Wear 273, 2011, 9-16.

5. E. Huttunen-Saarivirta, L. Kilpi, T.J. Hakala, L. Carpen, H. Ronkainen, Tribocorrosion study of martensitic and austenitic stainless steels in 0.01 M NaCl solution. Tribology International 95, 2016, 358-371.

6. E. Huttunen-Saarivirta, V. Heino, E. Isotahdon, L. Kilpi, H. Ronkainen, Tribocorrosion behaviour of thermally sprayed cermet coatings in paper machine environment. Tribology International 142, 2020, 106006.

7. A. Mäntyranta, V. Heino, E. Isotahdon, T. Salminen, E. Huttunen-Saarivirta, Tribocorrosion behaviour of two low-alloy steel grades in simulated waste solution. Tribology International 138, 2019, 250-262.

8. D. Landolt, S. Mischler, M. Stemp, Electrochemical methods in tribocorrosion: a critical appraisal. Electrochimica Acta 46, 2001, 3913-3929.

9. S. Mischler, Triboelectrochemical techniques and interpretation methods in tribocorrosion: A comparative evaluation. Tribology International 41, 2008, 573-583.

10. S.W. Watson, F.J. Friedersdorf, B.W. Madsen, S.D. Cramer, Methods of measuring wear-corrosion synergism. Wear 181-183, 1995, 476-484.

11. J.-P. Celis, P. Ponthiaux, F. Wenger, Tribo-corrosion of materials: Interplay between chemical, electrochemical, and mechanical reactivity of surfaces. Wear 261, 2006, 939-946.

12. G.H. Zhao, R.E. Aune, H. Mao, N. Espallargas, Degradation of Zr-based bulk metallic glasses used in load-bearing implants: A tribocorrosion appraisal. Journal of the Mechanical Behaviour of Biomedical Materials 60, 2016, 56-67.

13. R. Francis, Copper Alloys in Seawater: Avoidance of Corrosion. Copper Development Association Publication No 225, February 2016.

14. F.J.R. de Oliveira, D.C.B. Lago, L.F. Senna, L.R.M. de Miranda, E. D'Elia, Study of patina formation on bronze specimens. Materials Chemistry and Physics 115, 2009, 761-770.

15. J. Muller, B. Laik, I. Guillot, α-CuSn bronzes in sulphate medium: Influence of the tin content on corrosion processes. Corrosion Science 77, 2013, 46-51.

16. E. Sidot, N. Souissi, L. Bousselmi, E. Triki, L. Robbiola, Study of the corrosion behaviour of Cu-10Sn bronze in aerated Na_2SO_4 aqueous solution. Corrosion Science 48, 2006, 2241-2257.

17. D. Satovic, L. Valek Zulj, V. Desnica, S. Fazinic, S. Martinez, Corrosion evaluation and surface characterization of the corrosion product layer formed on Cu-6Sn bronze in aqueous Na_2SO_4 solution. Corrosion Science 51, 2009, 1593-1603.

18. F. Ammeloot, C. Fiaud, E.M.M. Sutter, Characterization of the oxide layers on a Cu-13Sn alloy in a NaCl aqueous solution without and with 0.1 M benzotriazole. Electrochemical and photoelectrochemical contributions. Electrochimica Acta 44, 1999, 2549-2558.

19. C. Debiemme-Chouvy, F. Ammeloot, E.M.M. Sutter, X-ray photoemission investigation of the corrosion film formed on a polished Cu-13Sn alloy in aerated NaCl solution. Applied Surface Science 174, 2001, 55-61.

20. N. Souissi, E. Sidot, L. Bousselmi, E. Triki, L. Robbiola, Corrosion behaviour of Cu-10Sn bronze in aerated NaCl aqueous media –Electrochemical investigation. Corrosion Science 49, 2007, 3333-3347.

21. L. Robbiola, T.T.M. Tran, P. Dupot, O. Majerus, K. Rahmouni, Characterisation of anodic layers on Cu-10Sn bronze (RDE) in aerated NaCl solution. Corrosion Science 50, 2008, 2205-2215.

22. E.R. Braithwaite, Solid lubricants and surfaces. Pergamon Press, New York, USA, 1964.

23. U. Ozsarac, F. Findik, M. Durman, The wear behaviour investigation of sliding bearings with a designed testing machine. Materials and Design 28, 2007, 345-350.

24. X. Guo, G. Zhang, W.-Y. Li, L. Dembinski, Y. Gao, H. Liao, C. Coddet, Microstructure, microhardness and dry friction behaviour of cold-sprayed tin bronze coatings. Applied Surface Science 254, 2007, 1482-1488.

25. E. Huttunen-Saarivirta, E. Isotahdon, J. Metsäjoki, T. Salminen, L. Carpén, H. Ronkainen, Tribocorrosion behaviour of aluminium bronze in 3.5 wt.% NaCl solution. Corrosion Science 144, 2018, 207-223.

26. E. Huttunen-Saarivirta, E. Isotahdon, J. Metsäjoki, T. Salminen, H. Ronkainen, L. Carpén, Behaviour of leaded tin bronze in simulated seawater in the absence and presence of tribological contact with alumina counterbody: Corrosion, wear and tribocorrosion. Tribology International 129, 2019, 257-271.

27. A. Lopez, R. Bayon, F. Pagano, A. Igartua, A. Arredondo, J.-L. Arana, J.J. Gonzalez, Tribocorrosion behaviour of mooring high strength low alloy steels in synthetic seawater. Wear 338-339, 2015, 1-10.

28. Y. Sun, V. Rana, Tribocorrosion behaviour of AISI 304 stainless steel in 0.5 M NaCl solution. Materials Chemistry and Physics 129, 2011, 138-147.

29. American Society for Testing and Materials (ASTM) International, G99-05: Standard test method for wear testing with a pin-on-disk apparatus. ASTM International, West Conshohocken, Pennsylvania, USA, 2016.

30. Y. Wang, L. Zhang, J. Xiao, W. Chen, C. Feng, X. Gan, K. Zhou, The tribo-corrosion behaviour of Cu-9wt.% Ni-6 wt.% Sn alloy. Tribology International 94, 2016, 260-268.

31. Cu-Sn, in T.B. Massalski (Ed.), Binary Alloy Phase Diagrams. ASM, Ohio, USA, 1986.

32. Cu-Sn system, available at: http://www.metallurgy.nist.gov/phase/solder/cusn.html (viewed on 17.02.2020).

33. N. Espallargas, R. Johnsen, C. Torres, A.I. Munoz, A new experimental technique for quantifying the galvanic coupling effects on stainless steel during tribocorrosion under equilibrium conditions. Wear 307, 2013, 190-197.

34. R.C.C. Silva, R.P. Nogueira, I.N. Bastos, Tribocorrosion of ENS S32750 in chloride medium: Effect of the load level. Electrochimica Acta 56, 2011, 8839-8845.

35. J. Takadoum, The influence of potential on the tribocorrosion of nickel and iron in sulphuric acid solution. Corrosion Science 38, 1996, 643-654.

36. J. Chen, J. Wang, F. Yan, Q. Zhang, Q. Li, Effect of applied potential on the tribocorrosion behaviours of Monel K500 alloy in artificial seawater. Tribology International 81, 2015, 1-8.

37. M. Ivanda, D. Waasmaier, A. Endriss, J. Ihringer, A. Kirfel, W. Kiefer, Low-Temperature Anomalies of Cuprite Observed by Raman Spectroscopy and X-Ray Powder Diffraction. Journal of Raman Spectroscopy 28, 1997, 487-493.

38. F. Ospitali, C. Chiavari, C. Martini, E. Bernardi, F. Passarini, L. Robbiola, The characterization of Sn-based corrosion products in ancient bronzes: a Raman approach. Journal of Raman Spectroscopy 43, 2012, 1596-1603.

39. H. Y. H. Chan, C. G. Takoudis, M. J. Weaver, Oxide Film Formation and Oxygen Adsorption on Copper in Aqueous Media As Probed by Surface-Enhanced Raman Spectroscopy. Journal of Physical Chemistry B 103, 1999, 357-365.

40. S.I. Pyun, Y.-G. Chun, Role of alloying elements tin and aluminium in anodic behaviour of homogeneous copper based alloys in 3-5 wt-% NaCl solution. British Corrosion Journal 31, 1996, 147-152.

Table captions

Table 1. Experimental conditions investigated in this research.

Table 2. Results from EDS analyses conducted for the specimens from pure corrosion tests. Values are given in wt.%.

Table 3. Results from EDS analyses conducted for the specimens from tribocorrosion tests. Values are given in wt.%.

Table 4. Hardness values, in MPa, measured after the tribocorrosion tests using nanoindentation (H_{IT}).

Figure captions

Figure 1. Optical microscopy images, showing the microstructure of tin bronze CuSn12 in a, b) a ground and polished condition, c, d) further etched with $FeCl_3$ etchant. The micrographs were taken at the direction perpendicular to the ingot longitudinal axis.

Figure 2. XRD spectra for the studied tin bronze a) in as-received condition and b-d) after corrosion tests. b) E = -200 mV vs. Ag/AgCl. c) E = 100 mV vs. Ag/AgCl. d) E = 500

mV vs. Ag/AgCl. In the spectra, the following marking of the identified phases is used: A=Cu, B=$Cu_{41}Sn_{11}$, C=Cu_2O, D=CuCl.

Figure 3. Results from OCP and potentiodynamic polarisation measurements using two concentrations of NaCl: 1.0 M and 0.01 M. a) OCP during the stabilisation period. b) Polarisation curves. c) Development of friction coefficient during the measurements.

Figure 4. Results from OCP and potentiodynamic polarisation measurements using two applied loads: 5 and 1 N, and compared with the situation without the load. a) OCP during the stabilisation period. b) Polarisation curves. c) Development of friction coefficient during the measurements.

Figure 5. The development of current density values during the potentiostatic tests without (corrosion) and with the applied load of 5 N (tribocorrosion, inert alumina counterbody). a) -200 mV vs. Ag/AgCl. b) 100 mV vs. Ag/AgCl. c) 500 mV vs. Ag/AgCl.

Figure 6. SEM images, showing the appearance of surfaces after the tests conducted in the absence of counterbody (corrosion) at various potentials. a, b) -200 mV vs. Ag/AgCl. c, d) 100 mV vs. Ag/AgCl. e, f) 500 mV vs. Ag/AgCl.

Figure 7. Optical microscopy images of the wear tracks in the disc specimens (a, c, e) and ball counterbodies (b, d, f). a, b) -200 mV vs. Ag/AgCl. c, d) 100 mV vs. Ag/AgCl. e, f) 500 mV vs. Ag/AgCl.

Figure 8. SEM images, showing the morphology of wear tracks in tin bronze specimens under the load of 5 N (tribocorrosion, inert alumina counterbody) at various potentials. a, b) -200 mV vs. Ag/AgCl. c, d) 100 mV vs. Ag/AgCl. e, f) 500 mV vs. Ag/AgCl.

Figure 9. Raman spectra for the wear tracks in tin bronze discs at various potentials. a) -200 mV vs. Ag/AgCl. b) 100 mV vs. Ag/AgCl. c) 500 mVvs. Ag/AgCl. Spectra show that all wear tracks are covered with Cu_2O, the peaks of which are indicated by ♦.

Figure 10. Friction coefficient records for tin bronze-inert alumina counterbody tribopair during potentiostatic experiments at the three potentials in 0.01 M NaCl solution under the load of 5 N.

Figure 11. Results from wear track cross-sectional studies. a) Examples of cross sections of the wear tracks, obtained by profilometry. b) Extent of material losses by the each of the degradation mechanism operating in the wear track. Solution: 0.01 M NaCl, inert alumina counterbody, 5 N load.

Figure 12. Results from OCP and potentiodynamic polarisation measurements with and without the reactive counterbody as well as only for the counterbody. a) OCP during the stabilisation period. b) Polarisation curves.

Figure 13. The development of current density values during the potentiostatic tests without (corrosion) and with the applied load of 5 N (tribocorrosion, reactive bearing steel

counterbody) at the anodic potentials for the tribopair. a) -275 mV. b) -150 mV. c) -50 mV.

Figure 14. SEM image of the wear track in tin bronze disc in contact with bearing steel pin at the potential of a) -400 mV. b) -275 mV. c) -150 mV. d) -50 mV.

Figure 15. SEM images, showing the wear track in bearing steel pin at different potentials. a) -400 mV. b) -275 mV. c) -150 mV. d) -50 mV. In b), the arrows indicate the transferred counterbody material in the disc surface,

Figure 16. Friction coefficient records for tin bronze during-reactive bearing steel counterbody tribopair in potentiostatic experiments at the four potentials in 0.6 M NaCl solution under the load of 5 N.

Figure 17. Results from degradation mechanism analyses. a) Examples of cross sections of the wear tracks, obtained by profilometry. b) Weight losses for the specimens during the experiments. Corrosion refers to experiments conducted for the tin bronze disc in the absence of (reactive steel) counterbody, whereas tribocorrosion refers to experiments carried out in the presence of the reactive steel counterbody. c) Results from chemical analyses of the test solutions after the experiments. Solution: 0.6 M NaCl, reactive bearing steel counterbody, 5 N load.

Table 1.

	Load, N	**Electrolyte NaCl concentration, M**	**Sliding speed, m/s**	**Potentials selected for potentiostatic experiments, mV vs. Ag/AgCl**	**Ways of characterizing material loss**
Inert counterbody	0, (1), 5	0.01, (1.0)	0.1	-200, 100, 500	Wear track cross section
Reactive counterbody	0, 5	0.6	0.2	-400, -275, -150, -50	Wear track cross section, weight change, electrolyte composition

Table 2.

Potential, mV vs. Ag/AgCl	***Area***	***O***	***Si***	***Cl***	***Cu***	***Sn***
-200	1	1.5			90.5	8.0
	2	1.0			72.6	26.4
100	*3*	14.0		2.9	72.9	10.1
	4	6.0		0.8	75.4	17.8
	5	1.3		37.2	60.7	0.5
500	*6*	22.0	1.0	2.2	73.0	1.8
	7	6.4		21.9	70.6	1.1
	8	30.5	1.5	1.2	66.8	

Table 3.

Potential, mV vs. Ag/AgCl	***Area***	***O***	***Si***	***P***	***Cl***	***Cu***	***Sn***
-200	1	8.5			0.2	87.8	3.5
	2	9.0			0.4	86.6	4.0
100	3	14.0	0.9		0.5	72.6	12.0
	4	8.6	0.3		0.5	81.4	9.3
500	*5*	15.6			5.9	70.8	7.7
	6	19.0		0.2	9.2	48.4	23.2

Table 4.

	-200 mV	***100 mV***	***500 mV***
Wear track	1870, σ = 515	813, σ = 182	473, σ = 186
Elsewhere	2757, σ = 316	2721, σ = 624	457, σ = 217

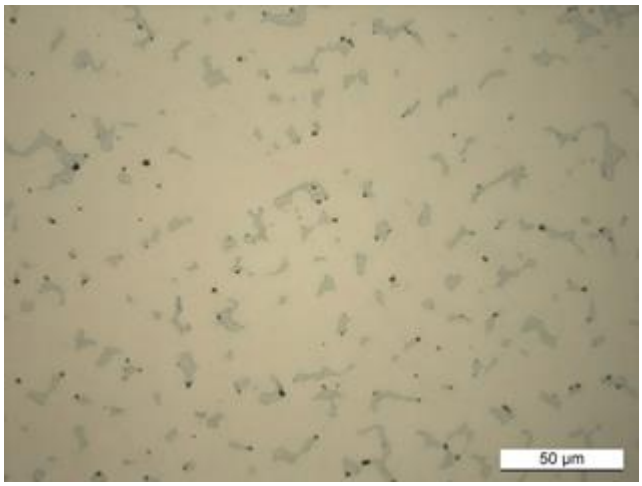

a)

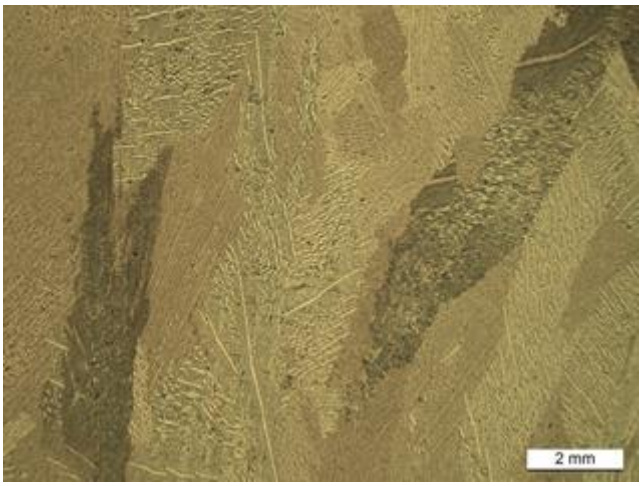

b)

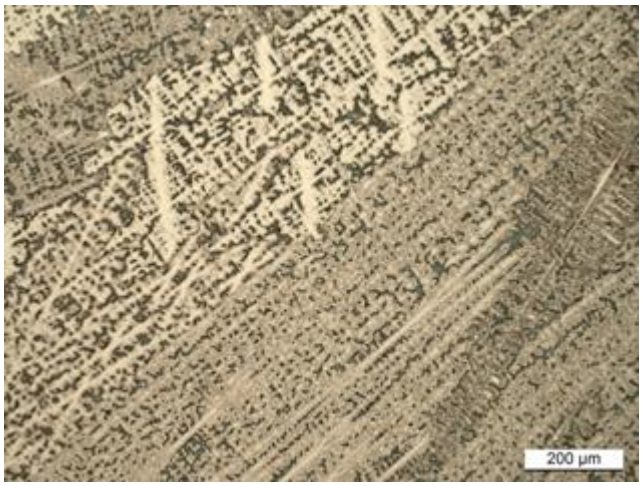

c)

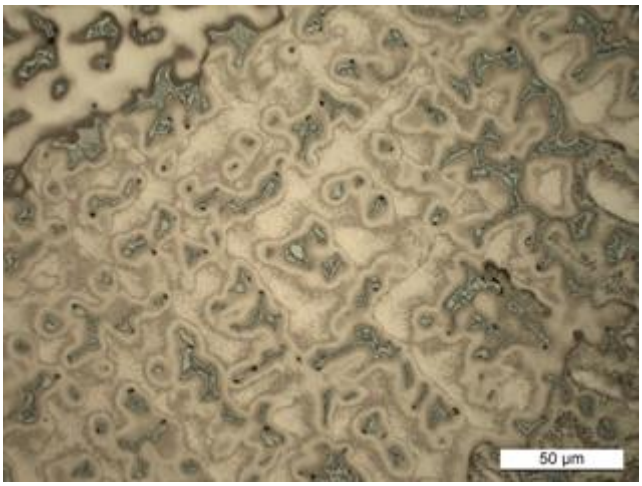

d)

Figure 1.

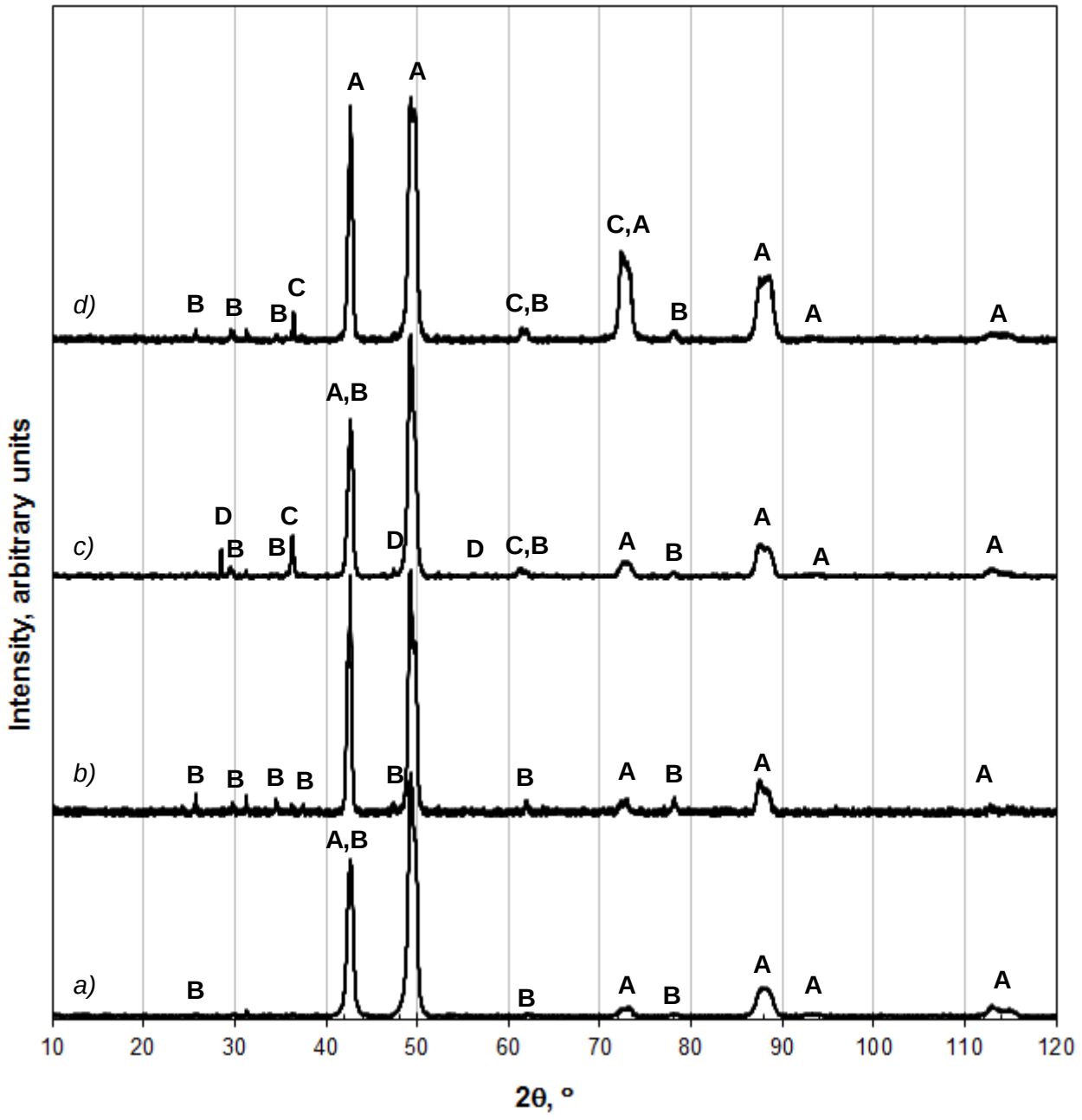
Intensity, arbitrary units
2θ, °
10
20
30
40
50
60
70
80
90
100
110
120
a)
b)
c)
d)
A
B
C
D
A,B
C,A
C,B

Figure 2.

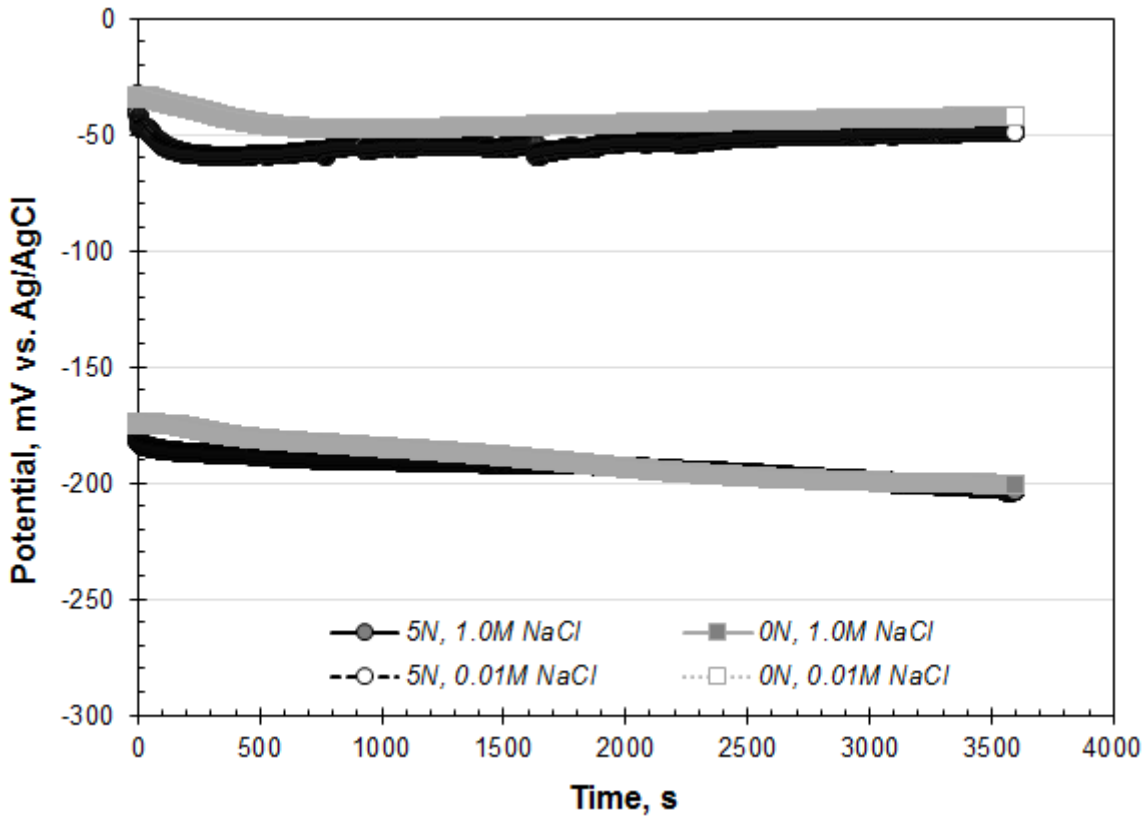
Potential, mV vs. Ag/AgCl
0
-50
-100
-150
-200
-250
-300
0
500
1000
1500
2000
2500
3000
3500
4000
Time, s
5N, 1.0M NaCl
0N, 1.0M NaCl
5N, 0.01M NaCl
0N, 0.01M NaCl

a)

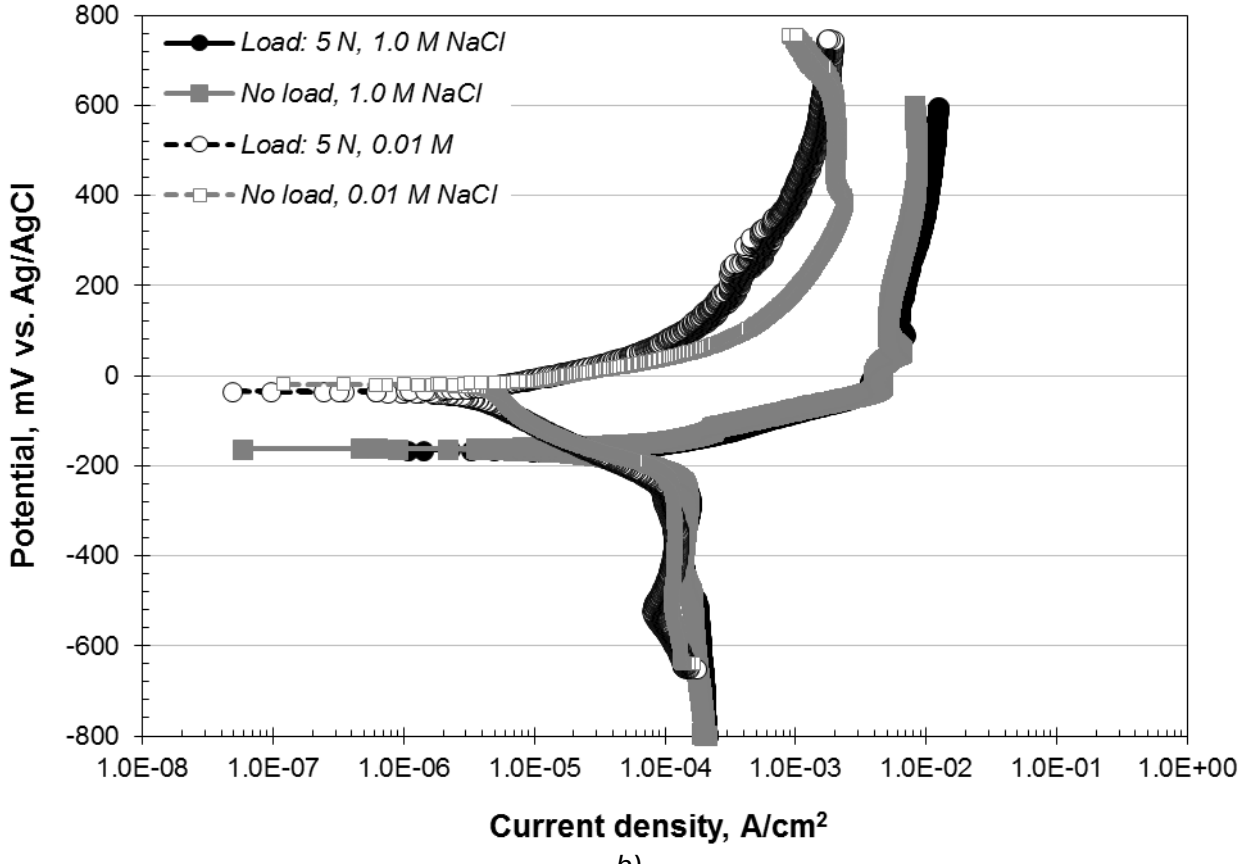
Potential, mV vs. Ag/AgCl
800
600
400
200
0
-200
-400
-600
-800
1.0E-08
1.0E-07
1.0E-06
1.0E-05
1.0E-04
1.0E-03
1.0E-02
1.0E-01
1.0E+00
Current density, A/cm2
Load: 5 N, 1.0 M NaCl
No load, 1.0 M NaCl
Load: 5 N, 0.01 M
No load, 0.01 M NaCl

b)

Figure 3.

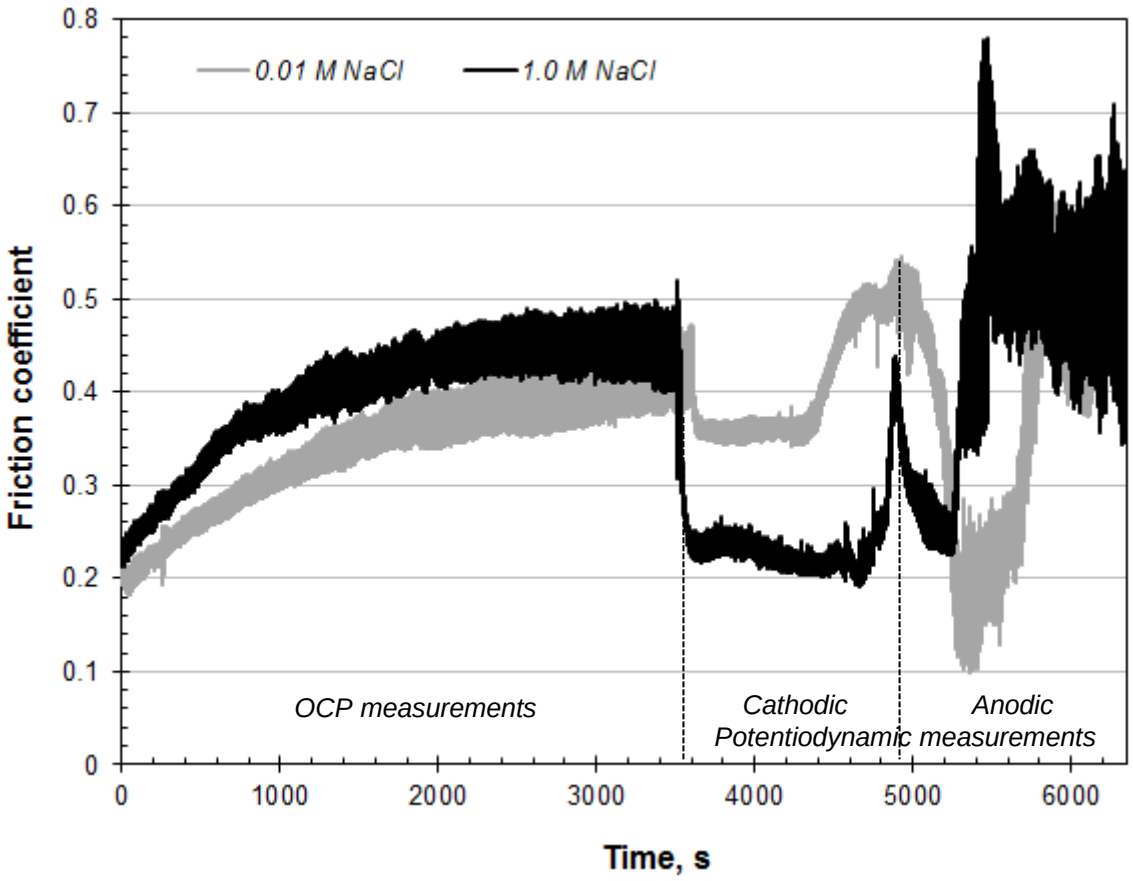
0.01 M NaCl
1.0 M NaCl
Friction coefficient
0.8
0.7
0.6
0.5
0.4
0.3
0.2
0.1
0
0
1000
2000
3000
4000
5000
6000
Time, s
OCP measurements
Cathodic
Potentiodynamic measurements
Anodic

c)

Figure 3.

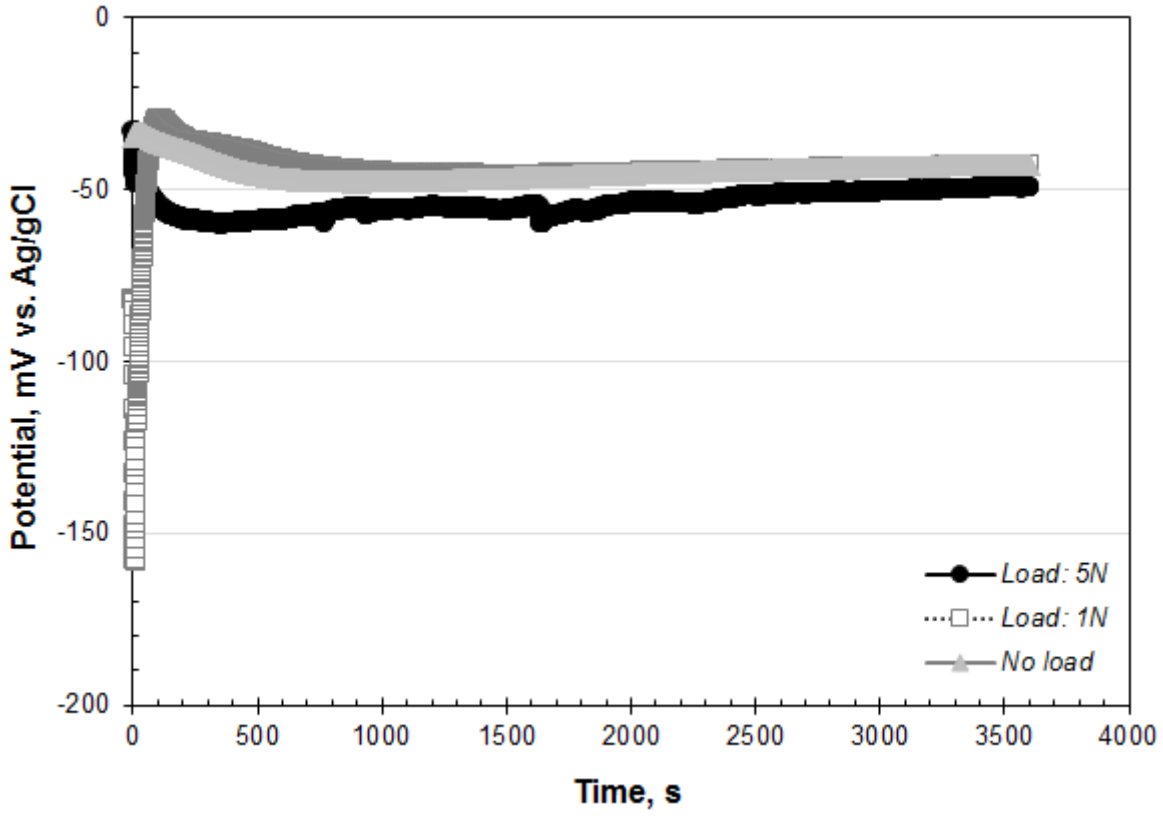
Potential, mV vs. Ag/gCl
0
-50
-100
-150
-200
0
500
1000
1500
2000
2500
3000
3500
4000
Time, s
Load: 5N
Load: 1N
No load

a)

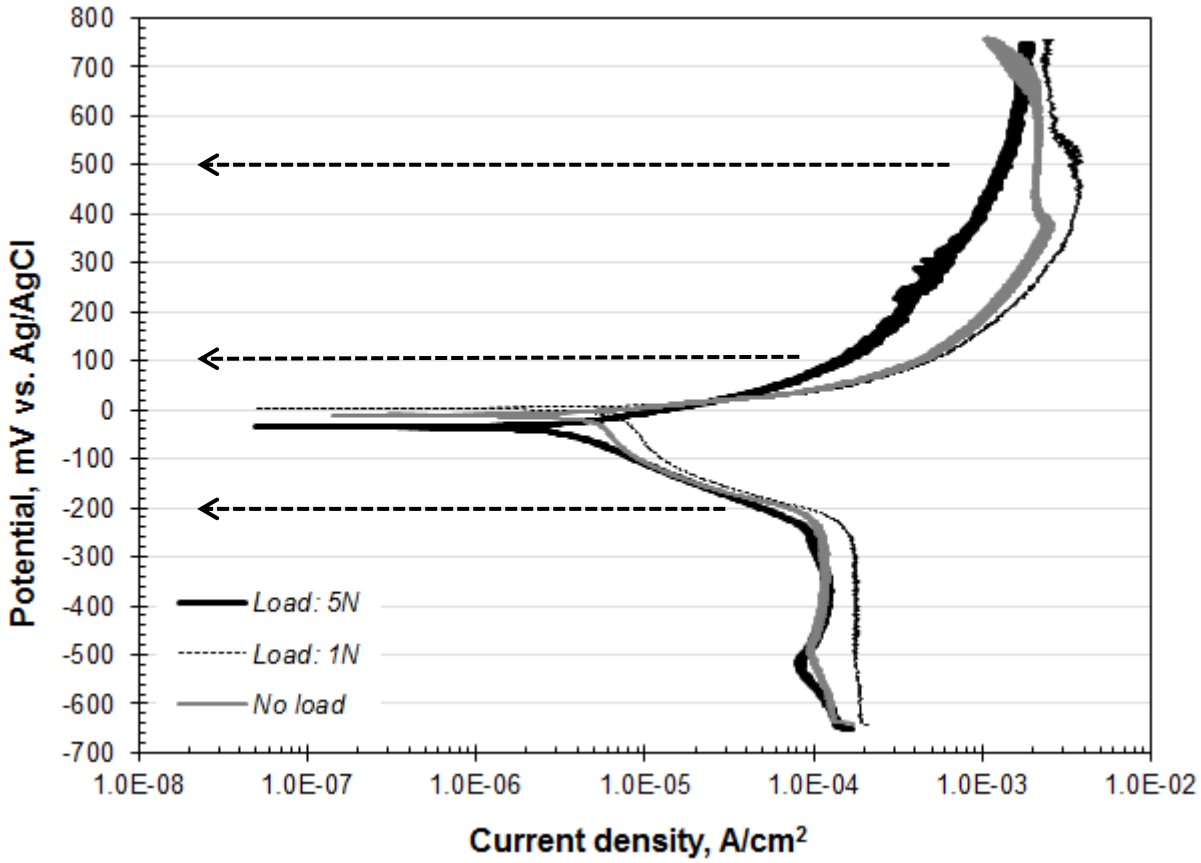
Potential, mV vs. Ag/AgCl
800
700
600
500
400
300
200
100
0
-100
-200
-300
-400
-500
-600
-700
1.0E-08
1.0E-07
1.0E-06
1.0E-05
1.0E-04
1.0E-03
1.0E-02
Current density, A/cm2
Load: 5N
Load: 1N
No load

b)

Figure 4.

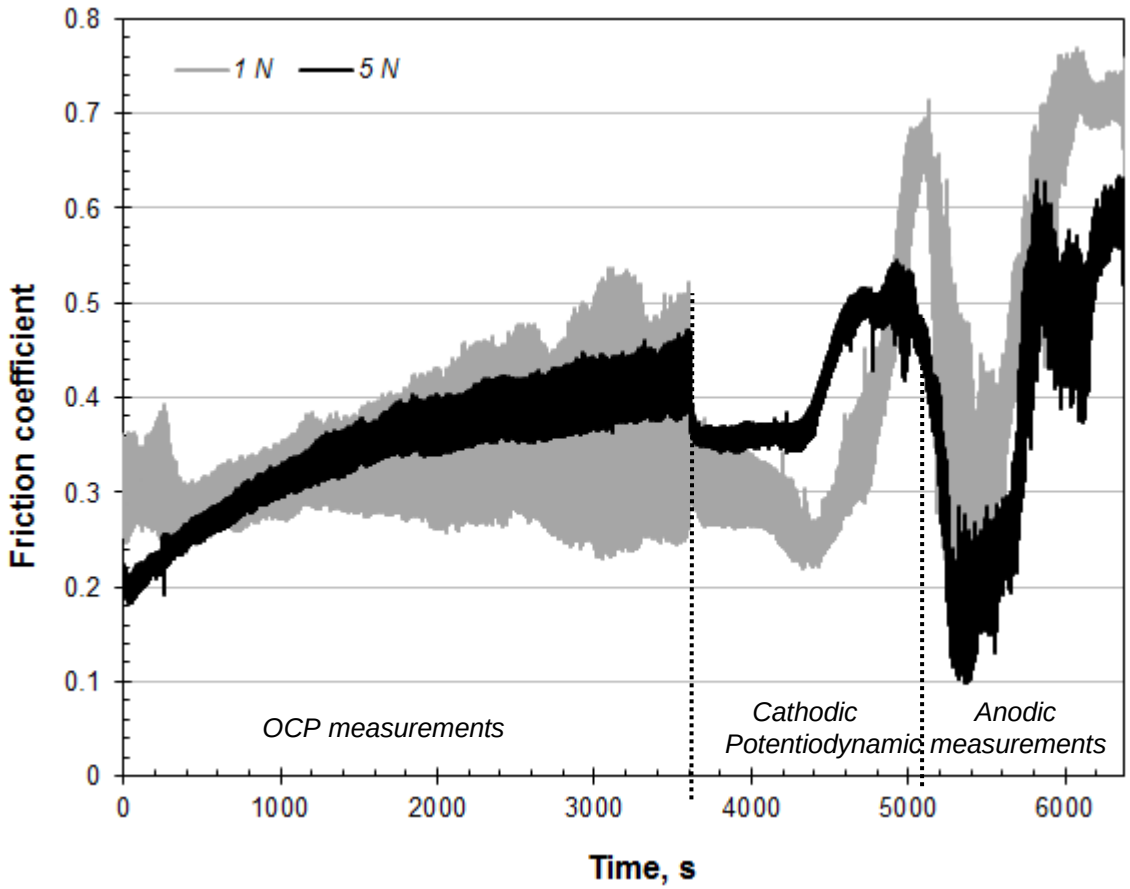
1 N
5 N
Friction coefficient
0.8
0.7
0.6
0.5
0.4
0.3
0.2
0.1
0
0
1000
2000
3000
4000
5000
6000
Time, s
OCP measurements
Cathodic Potentiodynamic
Anodic measurements

c)

Figure 4.

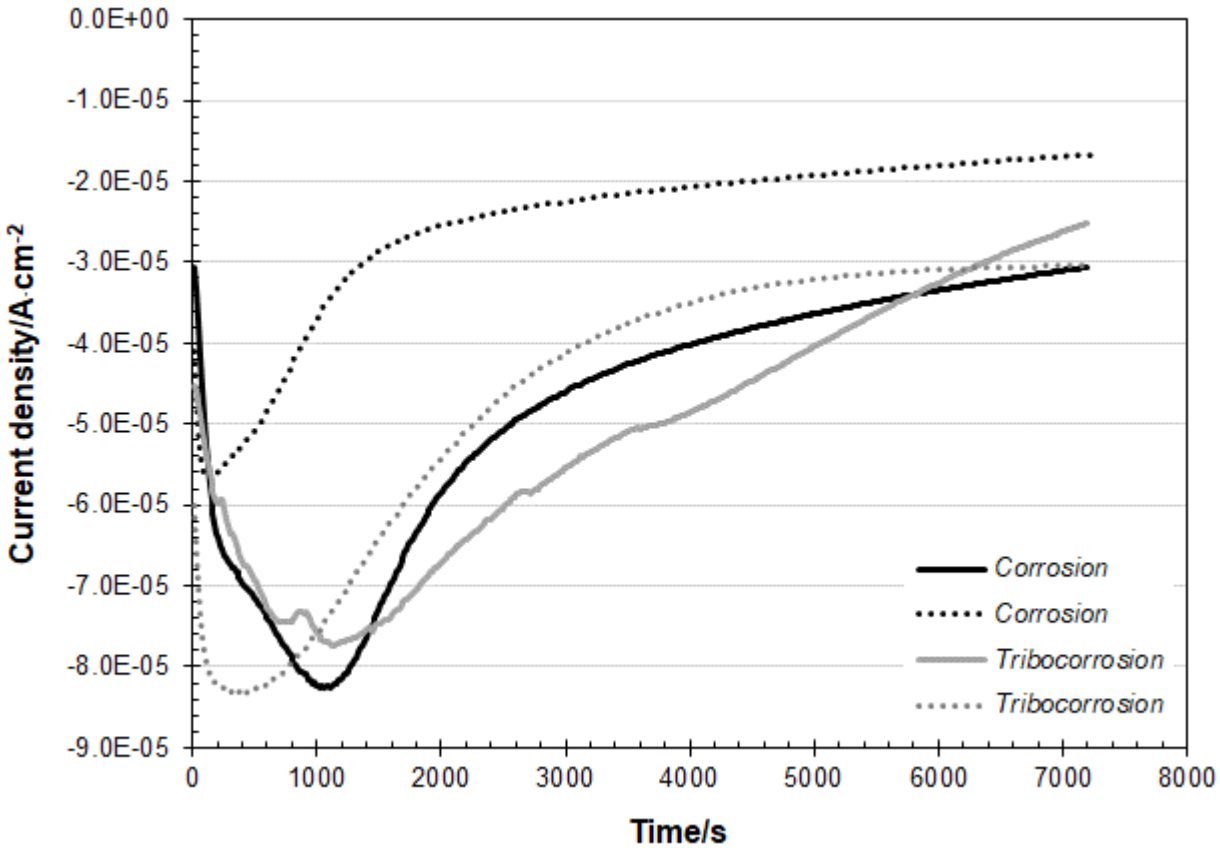
0.0E+00
-1.0E-05
-2.0E-05
-3.0E-05
-4.0E-05
-5.0E-05
-6.0E-05
-7.0E-05
-8.0E-05
-9.0E-05
Current density/A·cm⁻²
0
1000
2000
3000
4000
5000
6000
7000
8000
Time/s
Corrosion
Corrosion
Tribocorrosion
Tribocorrosion

a)

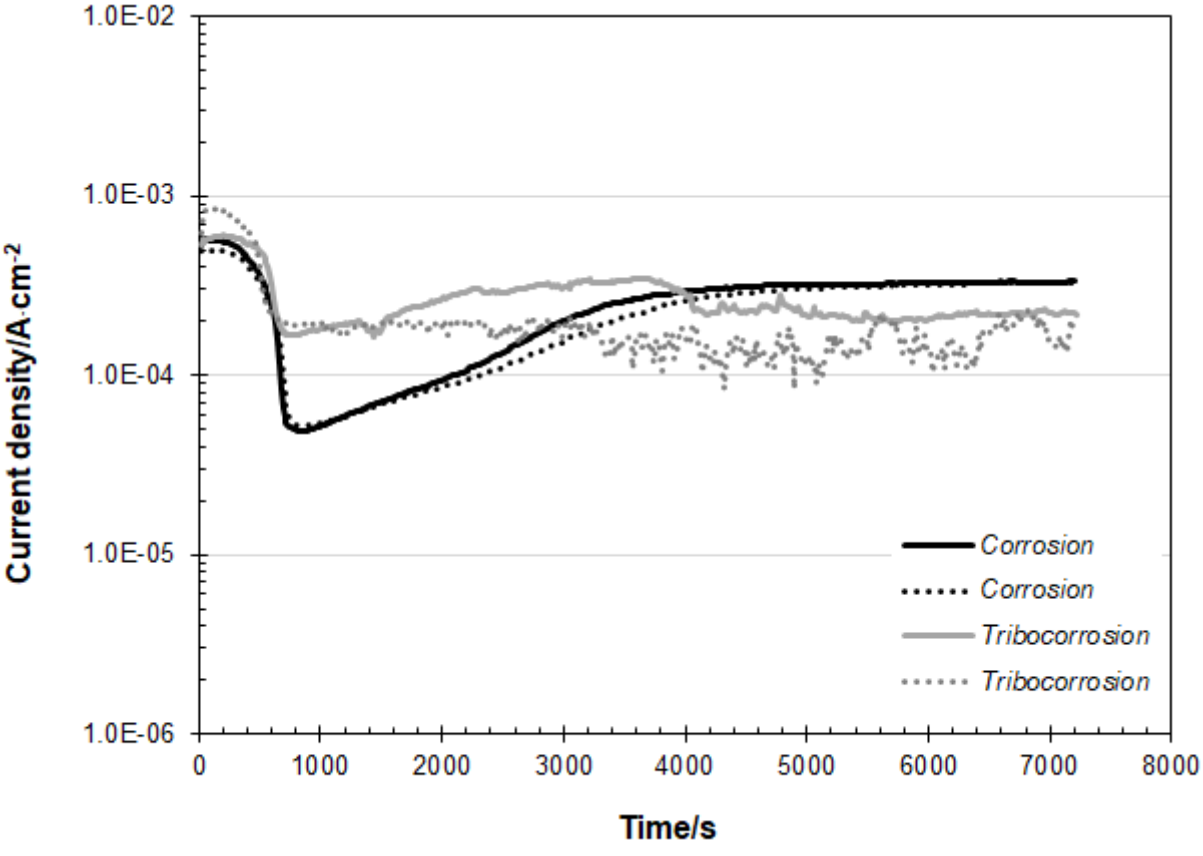
1.0E-02
1.0E-03
1.0E-04
1.0E-05
1.0E-06
Current density/A·cm⁻²
0
1000
2000
3000
4000
5000
6000
7000
8000
Time/s
Corrosion
Corrosion
Tribocorrosion
Tribocorrosion

b)

Figure 5.

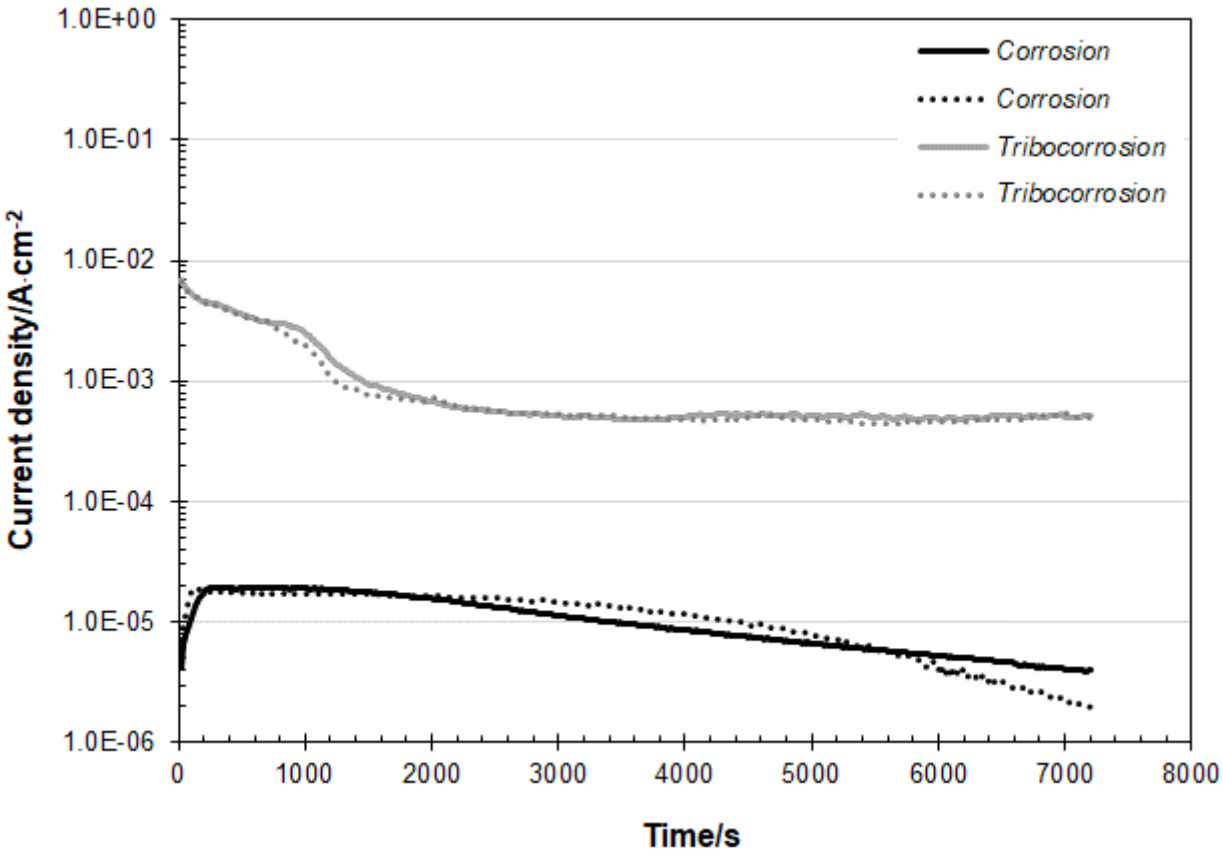
1.0E+00
1.0E-01
1.0E-02
1.0E-03
1.0E-04
1.0E-05
1.0E-06
Current density/A·cm⁻²
0
1000
2000
3000
4000
5000
6000
7000
8000
Time/s
Corrosion
Corrosion
Tribocorrosion
Tribocorrosion

c)

Figure 5.

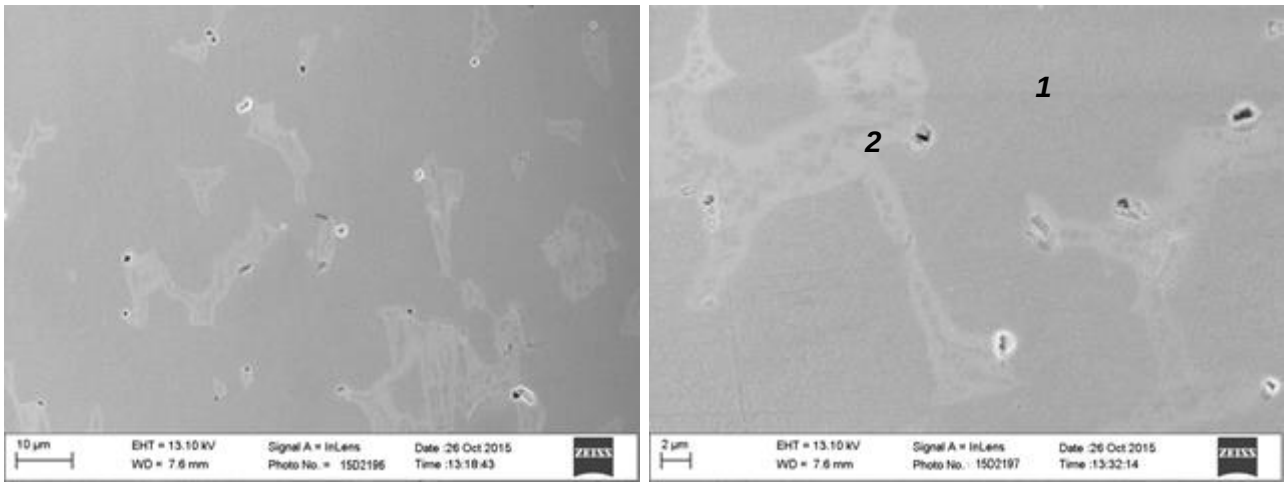

a) b)

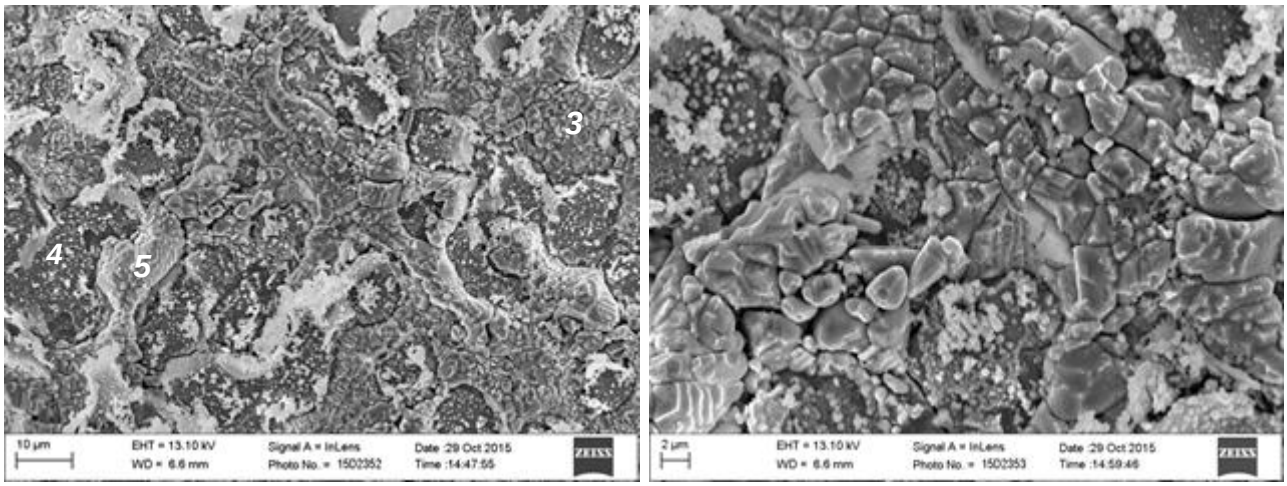

c) d)

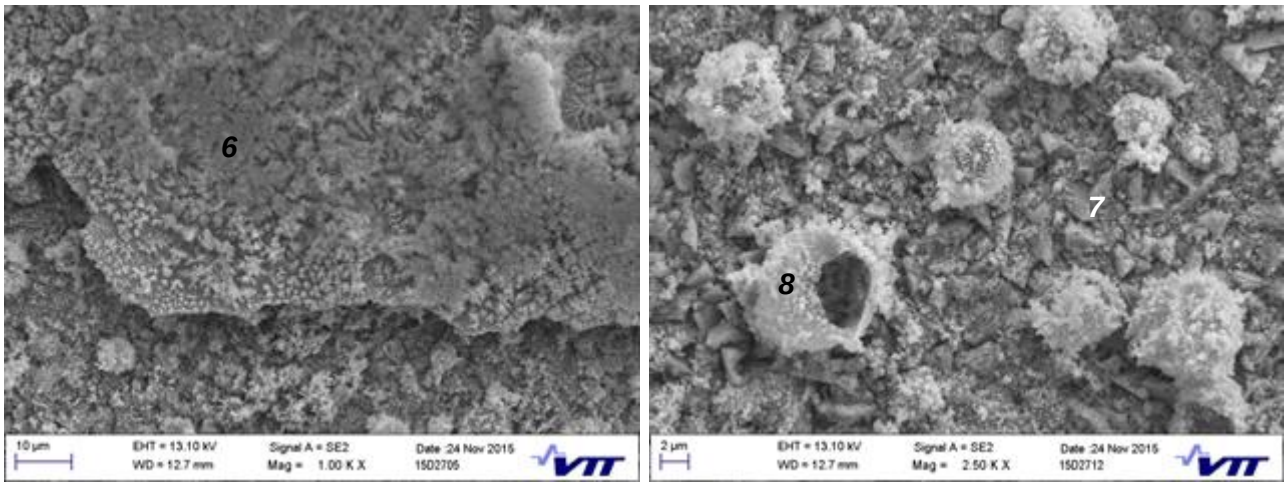

e) f)

Figure 6.

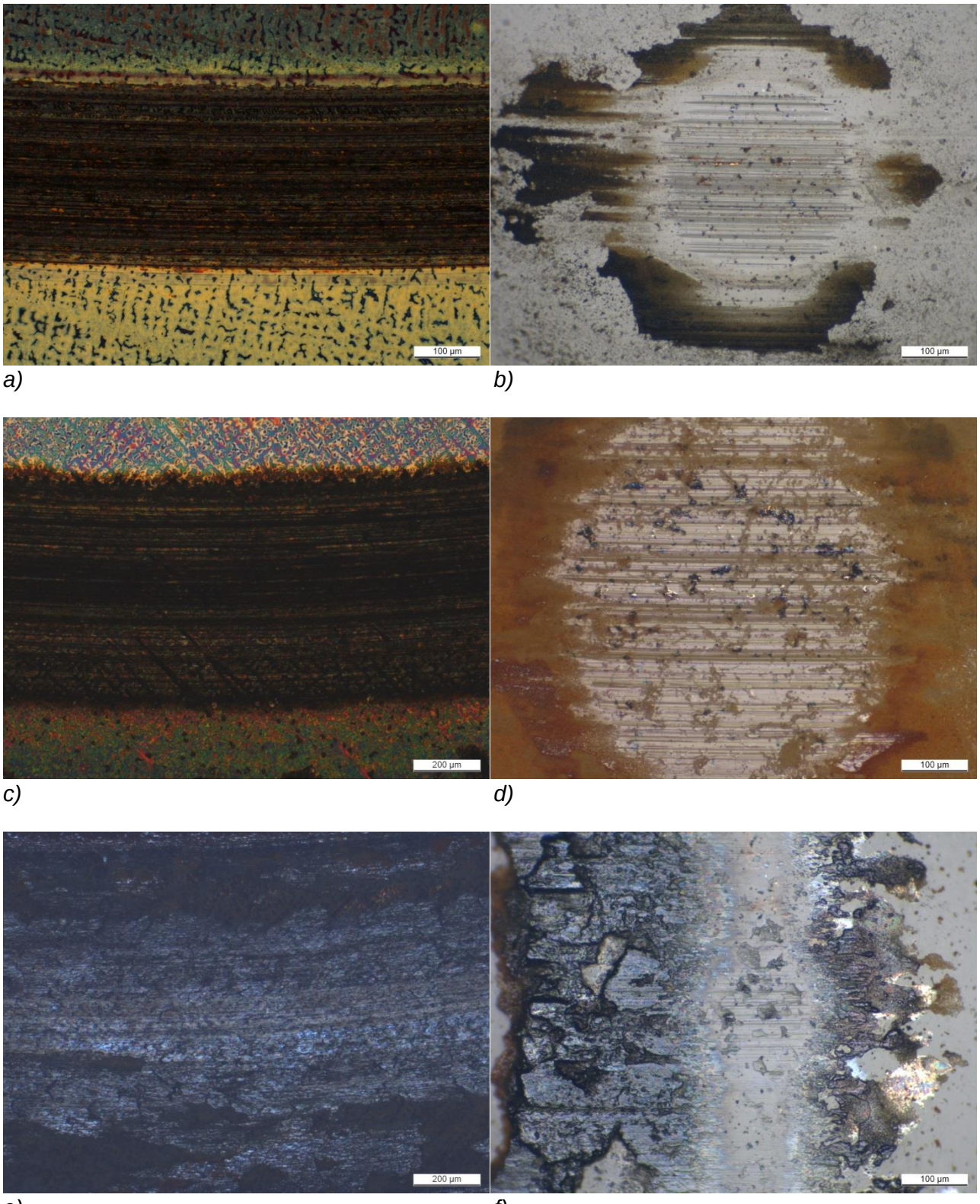

a) *b)*

c) *d)*

e) *f)*

Figure 7.

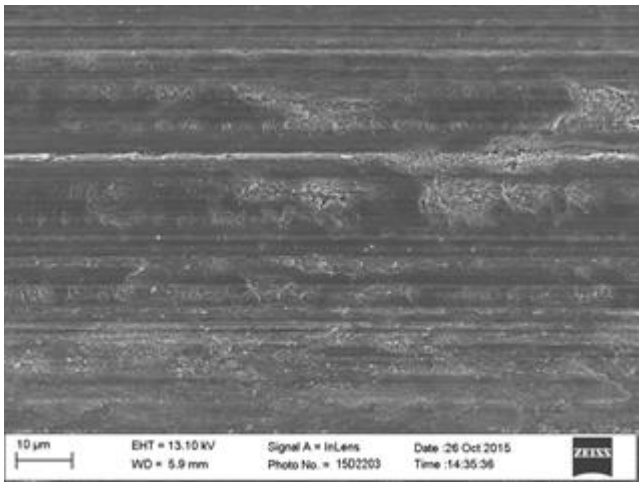

a)

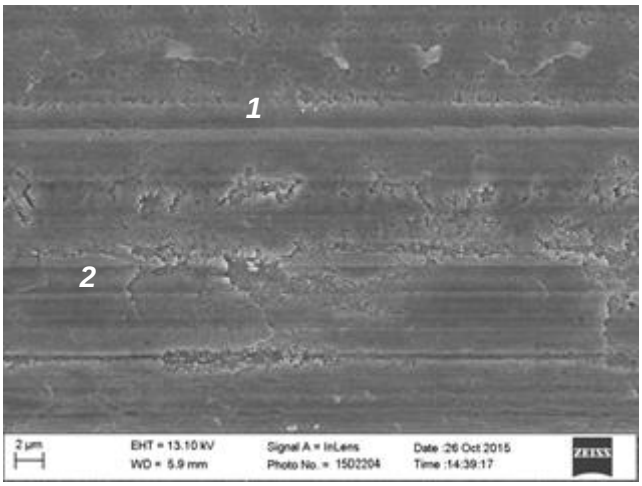

b)

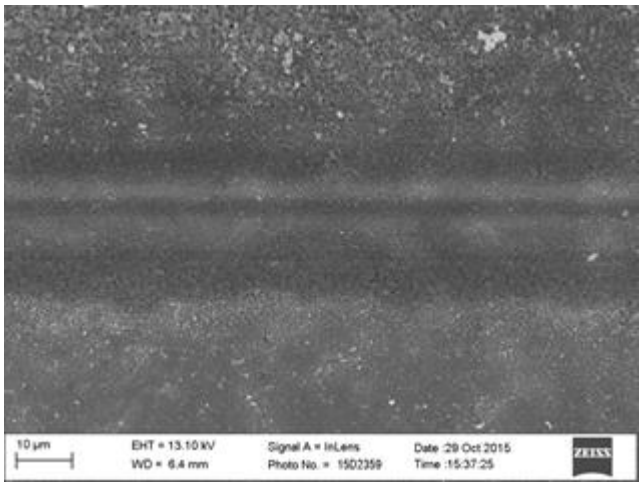

c)

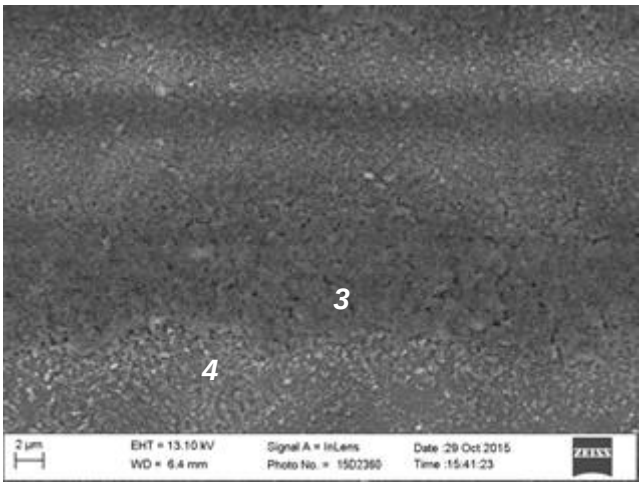

d)

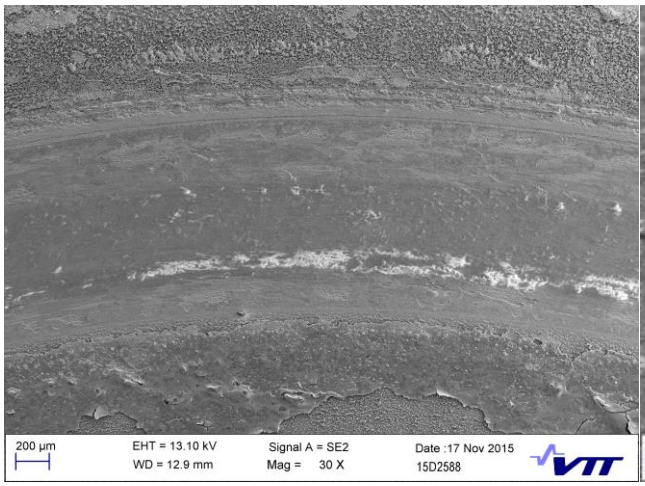

e)

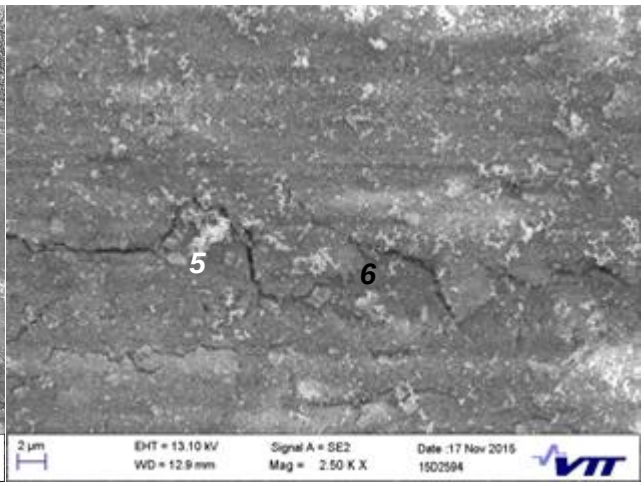

f)

Figure 8.

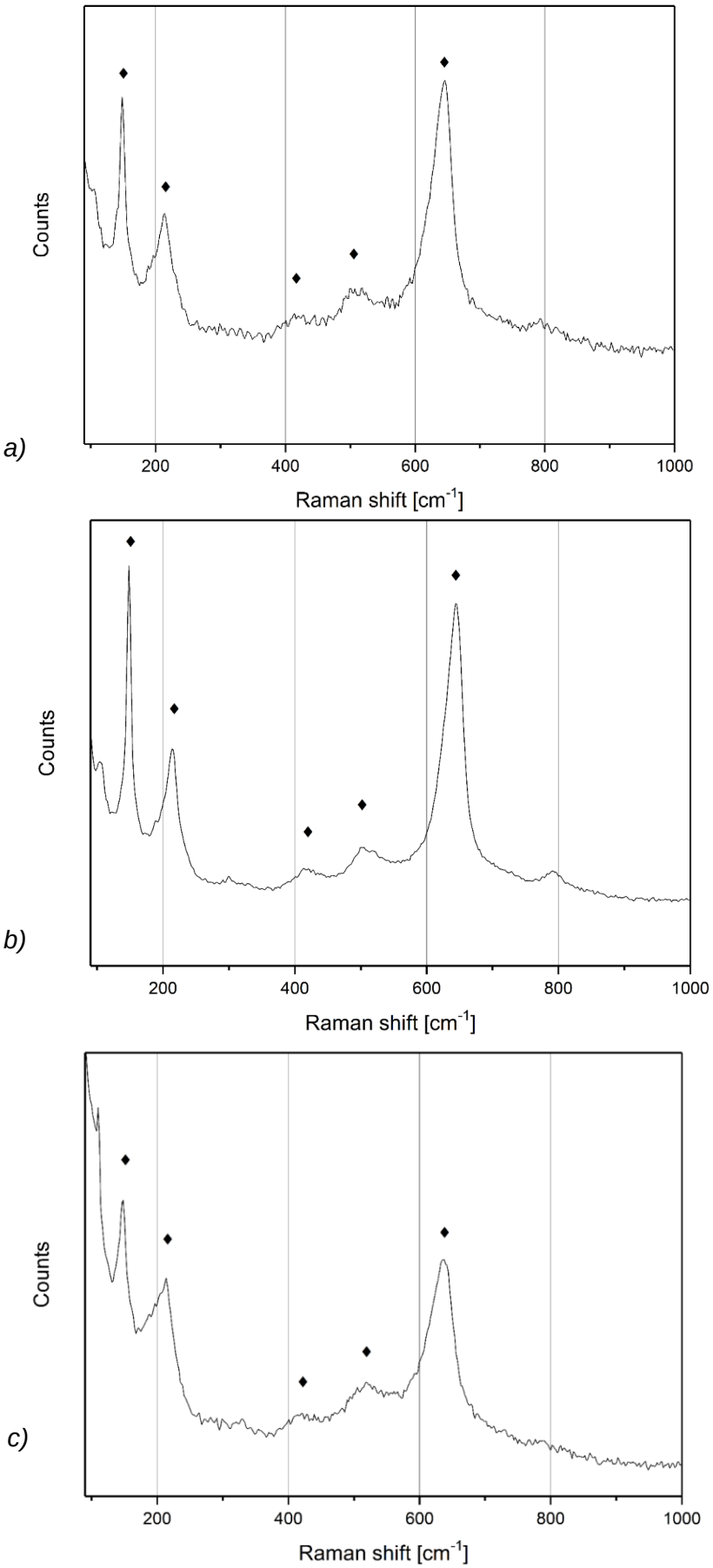
a)
Counts
200
400
600
800
1000
Raman shift [cm-1]
b)
Counts
200
400
600
800
1000
Raman shift [cm-1]
c)
Counts
200
400
600
800
1000
Raman shift [cm-1]

Figure 9.

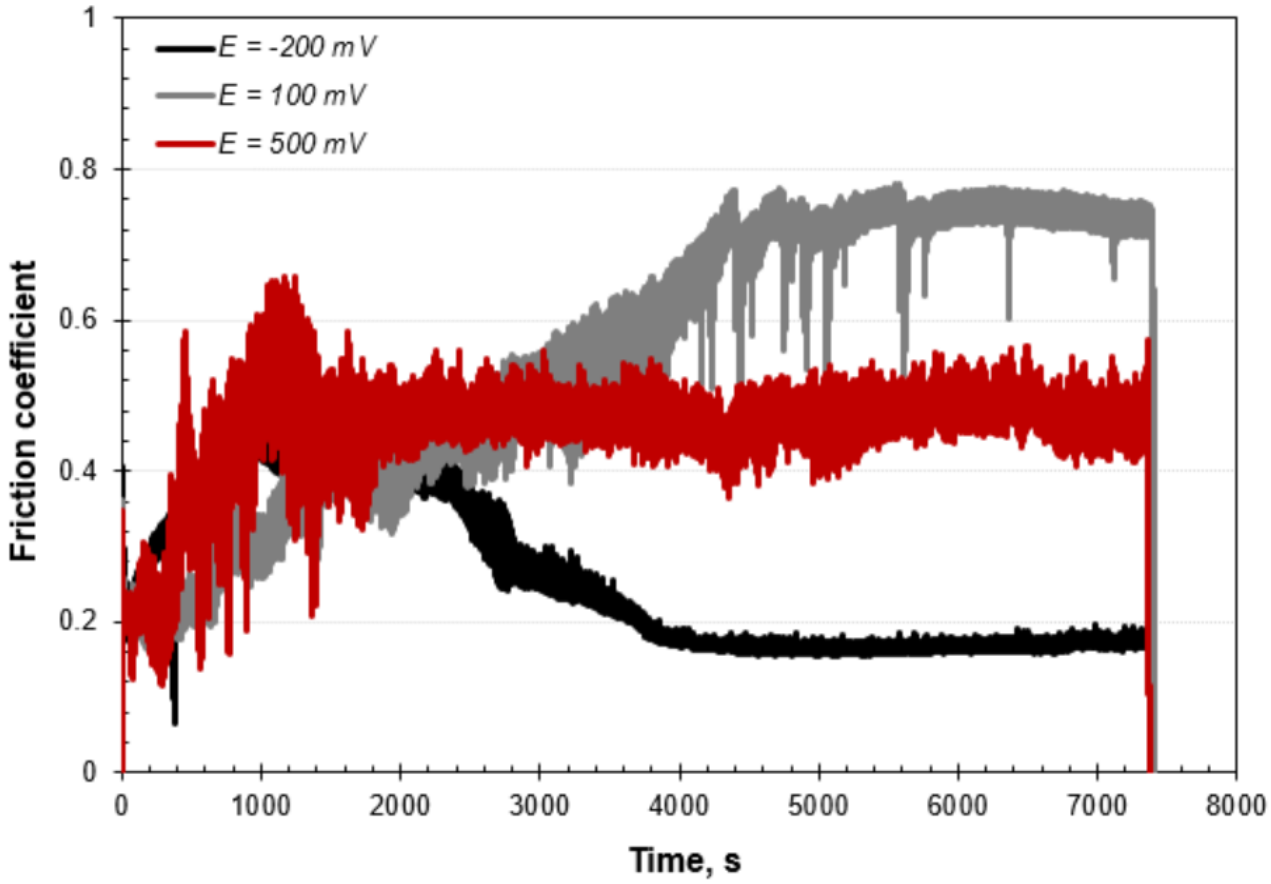
E = -200 mV
E = 100 mV
E = 500 mV
Friction coefficient
Time, s
0
0.2
0.4
0.6
0.8
1
0
1000
2000
3000
4000
5000
6000
7000
8000

Figure 10.

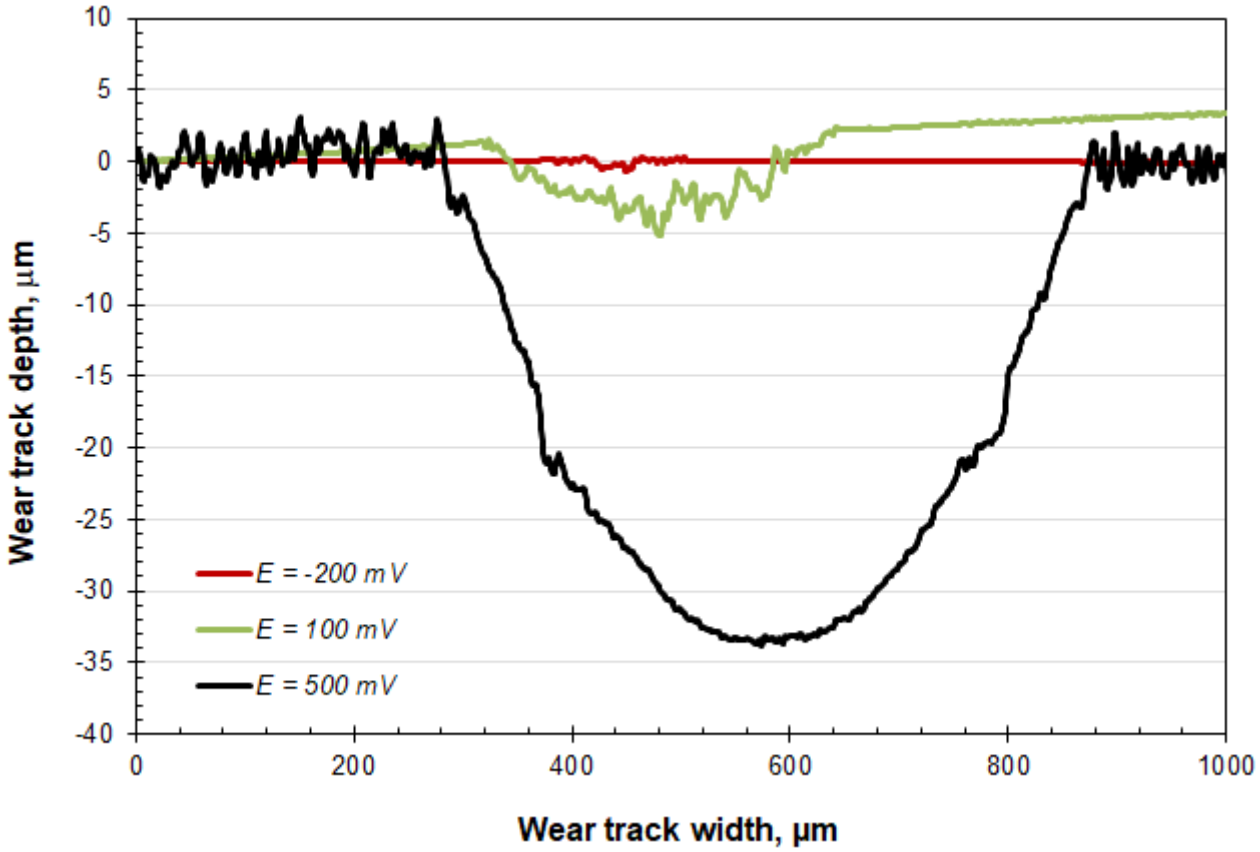
Wear track depth, µm
Wear track width, µm
E = -200 mV
E = 100 mV
E = 500 mV

a)

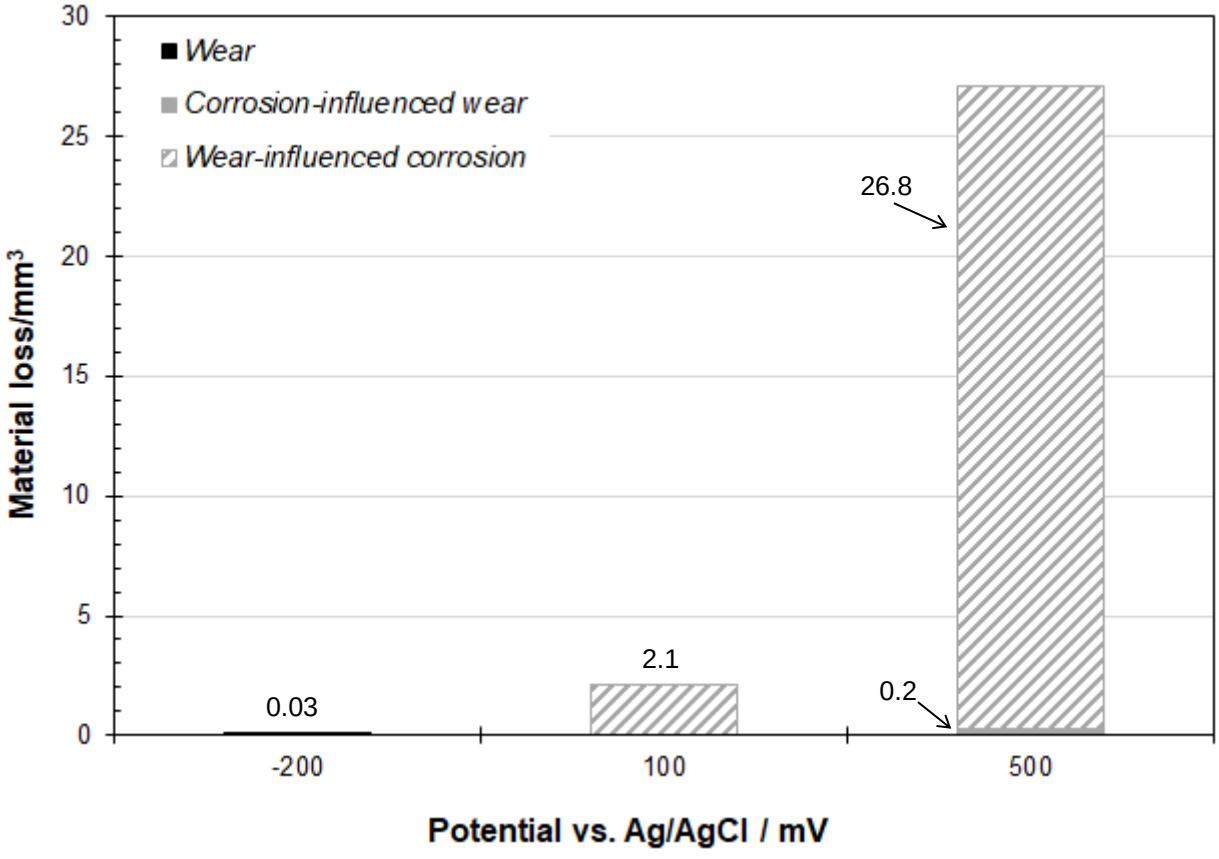
Material loss/mm³
Potential vs. Ag/AgCl / mV
Wear
Corrosion-influenced wear
Wear-influenced corrosion
0.03
2.1
26.8
0.2

b)

Figure 11.

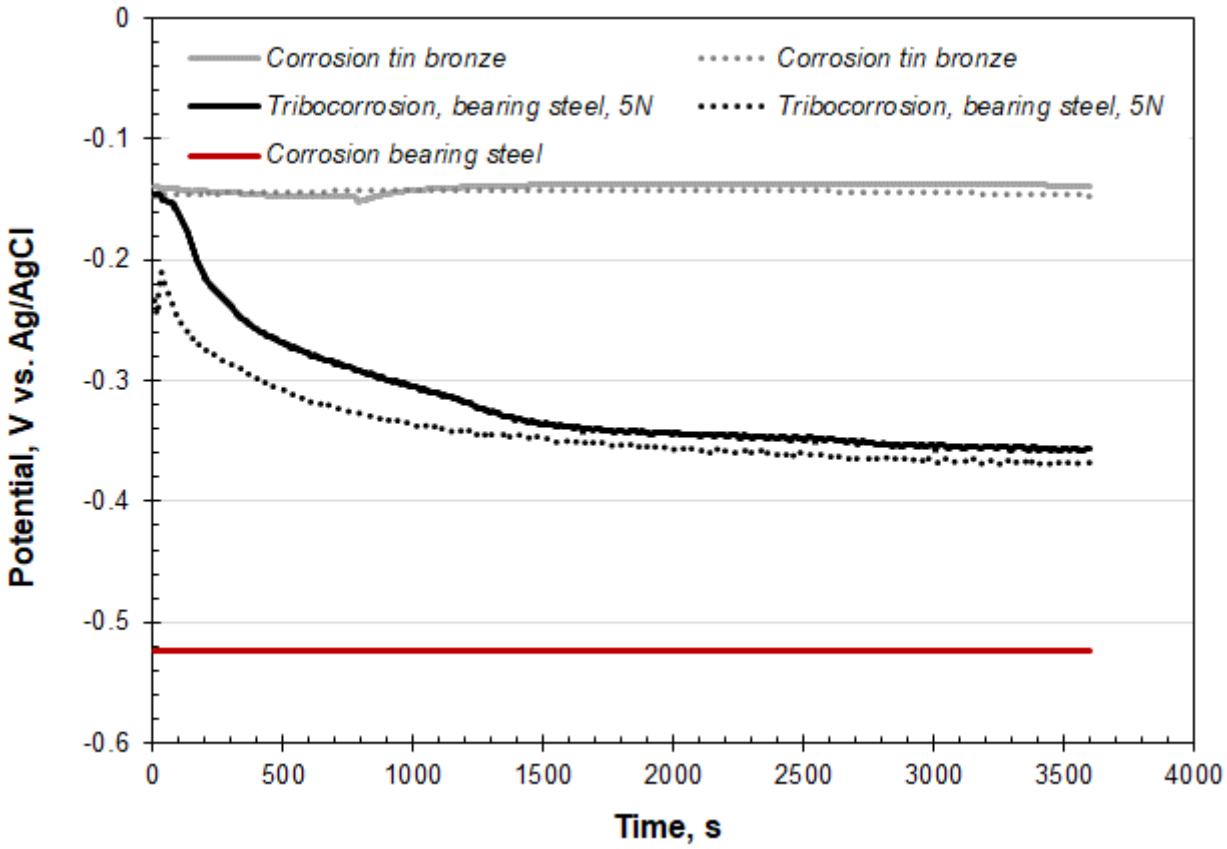
Corrosion tin bronze
Corrosion tin bronze
Tribocorrosion, bearing steel, 5N
Tribocorrosion, bearing steel, 5N
Corrosion bearing steel
Potential, V vs. Ag/AgCl
Time, s
0
-0.1
-0.2
-0.3
-0.4
-0.5
-0.6
0
500
1000
1500
2000
2500
3000
3500
4000

a)

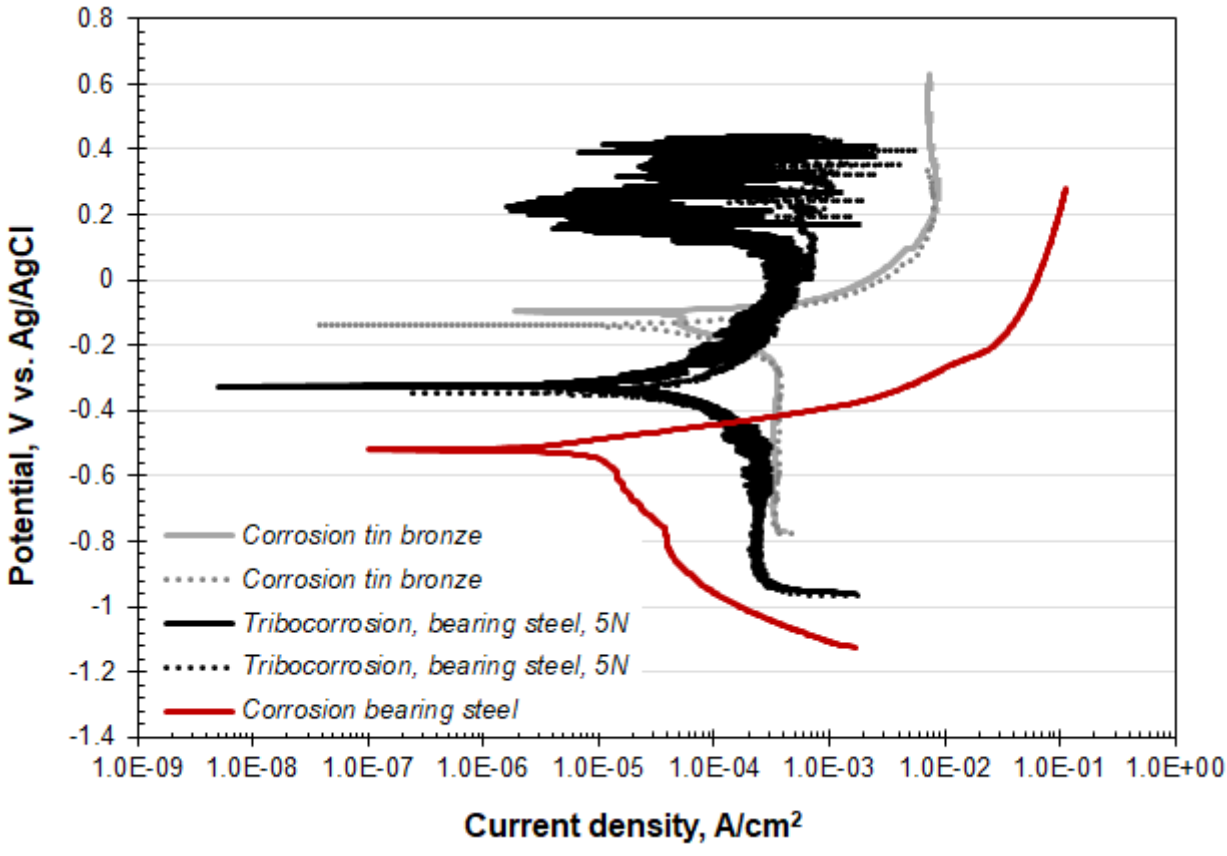
Corrosion tin bronze
Corrosion tin bronze
Tribocorrosion, bearing steel, 5N
Tribocorrosion, bearing steel, 5N
Corrosion bearing steel
Potential, V vs. Ag/AgCl
Current density, A/cm²
0.8
0.6
0.4
0.2
0
-0.2
-0.4
-0.6
-0.8
-1
-1.2
-1.4
1.0E-09
1.0E-08
1.0E-07
1.0E-06
1.0E-05
1.0E-04
1.0E-03
1.0E-02
1.0E-01
1.0E+00

b)

Figure 12.

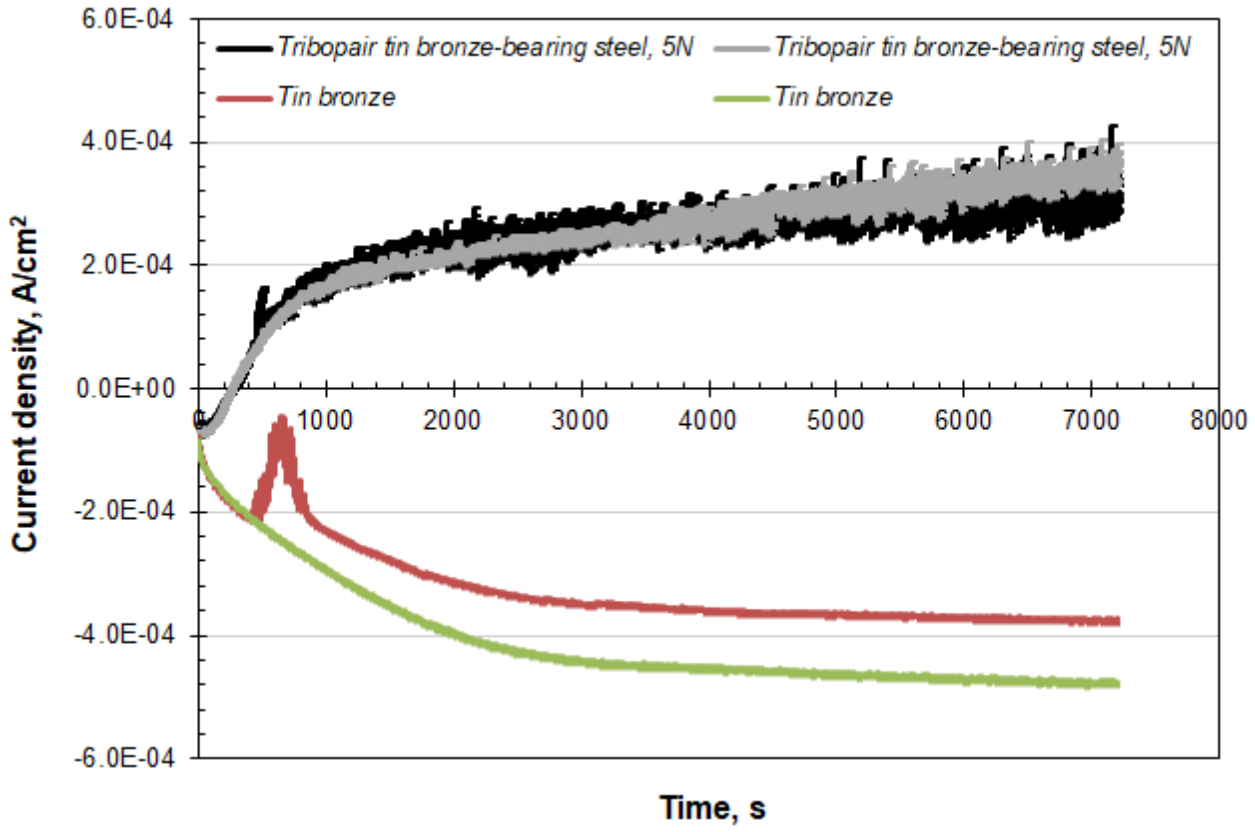
6.0E-04
4.0E-04
2.0E-04
0.0E+00
-2.0E-04
-4.0E-04
-6.0E-04
Current density, A/cm²
Tribopair tin bronze-bearing steel, 5N
Tribopair tin bronze-bearing steel, 5N
Tin bronze
Tin bronze
0
1000
2000
3000
4000
5000
6000
7000
8000
Time, s

a)

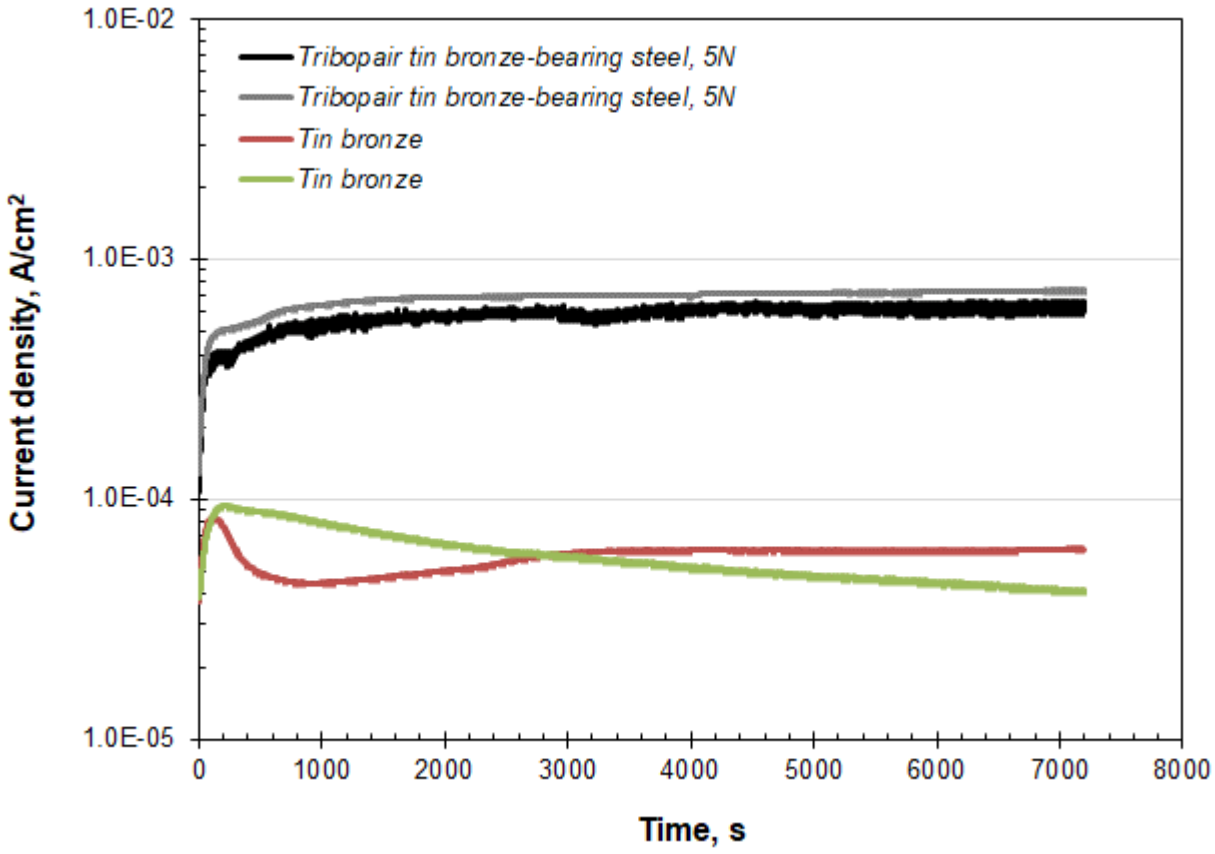
1.0E-02
1.0E-03
1.0E-04
1.0E-05
Current density, A/cm²
Tribopair tin bronze-bearing steel, 5N
Tribopair tin bronze-bearing steel, 5N
Tin bronze
Tin bronze
0
1000
2000
3000
4000
5000
6000
7000
8000
Time, s

b)

Figure 13.

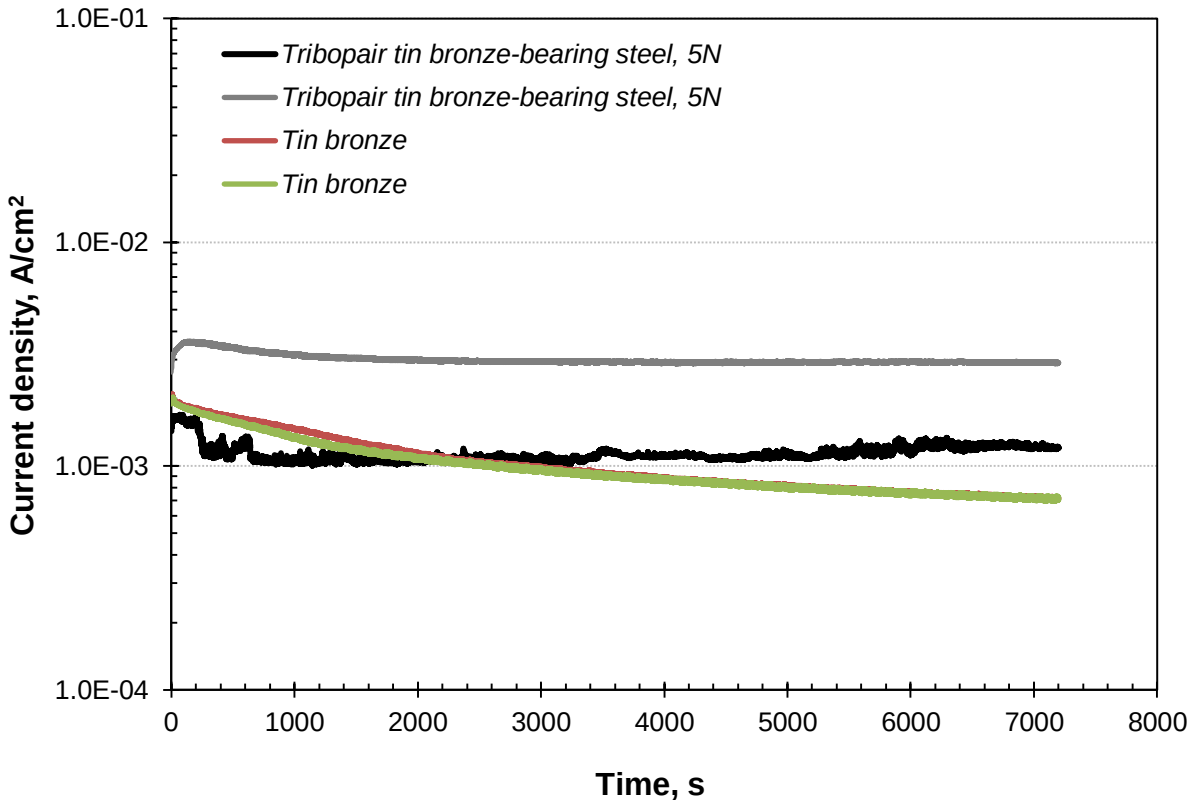
1.0E-01
1.0E-02
1.0E-03
1.0E-04
Current density, A/cm²
Tribopair tin bronze-bearing steel, 5N
Tribopair tin bronze-bearing steel, 5N
Tin bronze
Tin bronze
0
1000
2000
3000
4000
5000
6000
7000
8000
Time, s

c)

Figure 13.

a)

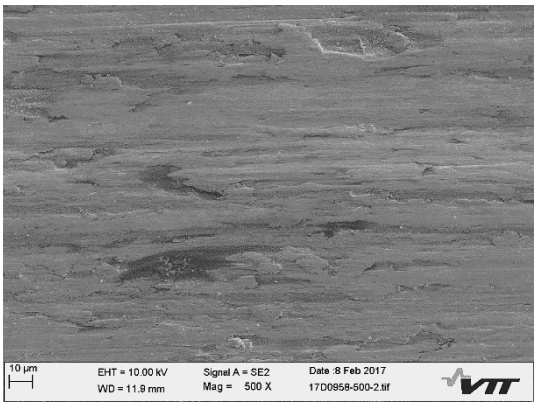

b)

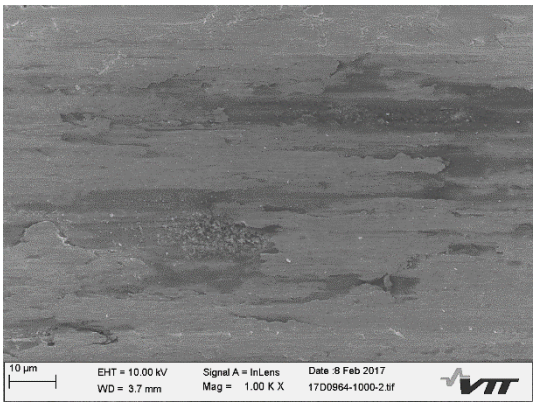

c)

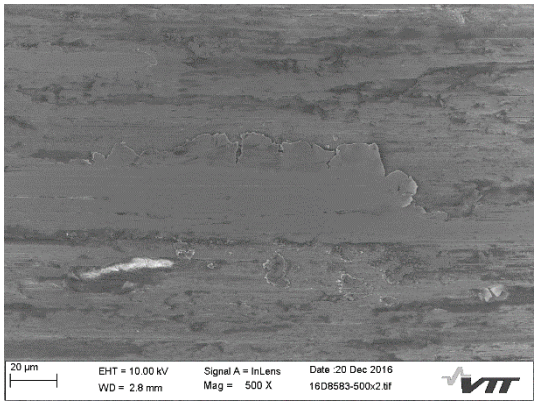

d)

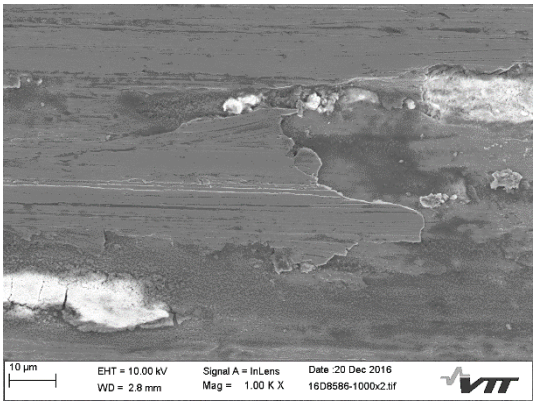

e)

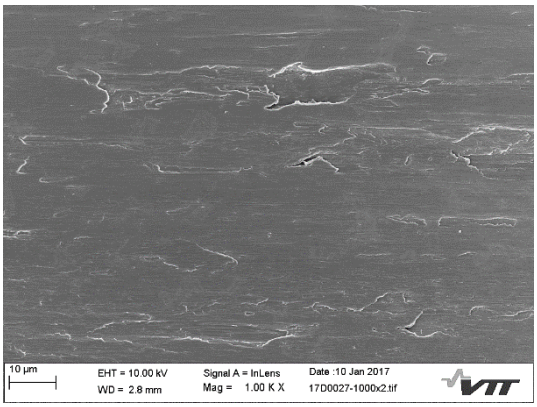

f)

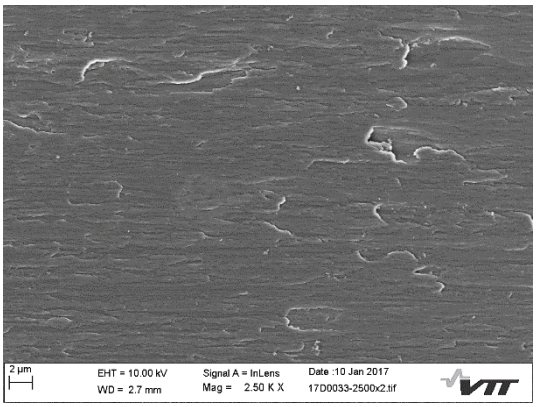

g)

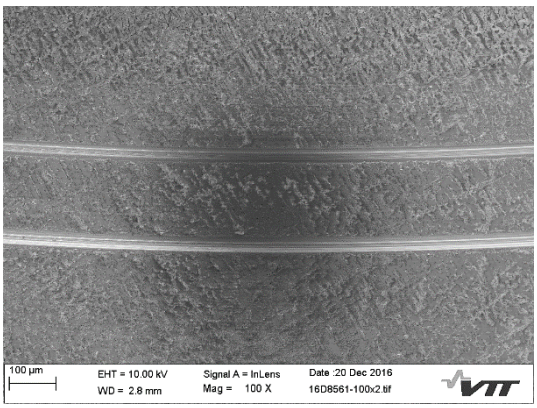

h)

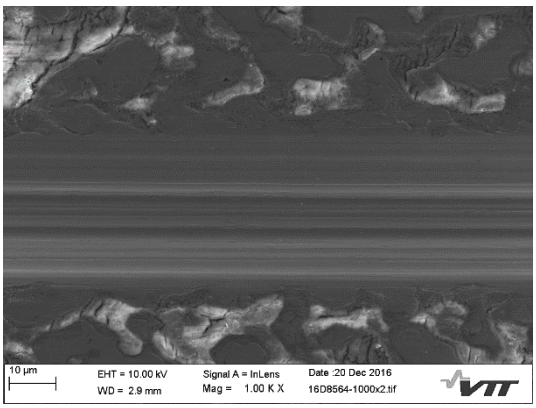

Figure 14.

a)

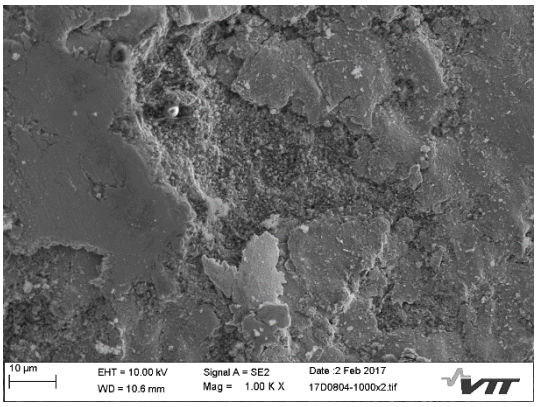

b)

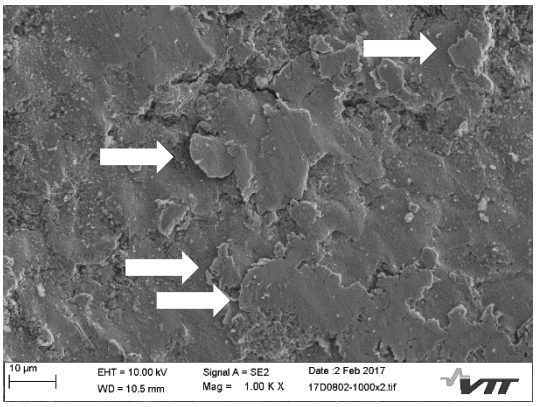

c)

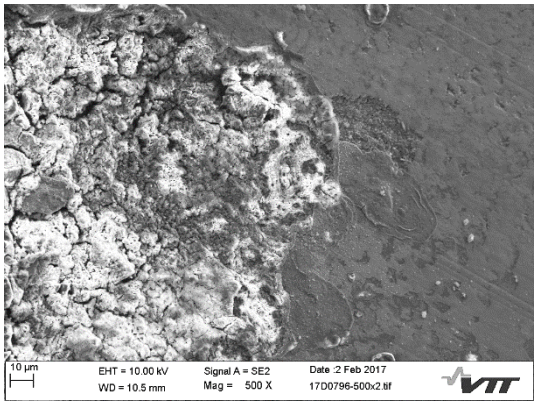

d)

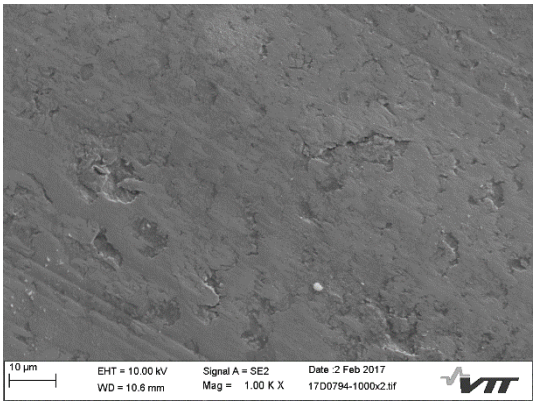

e)

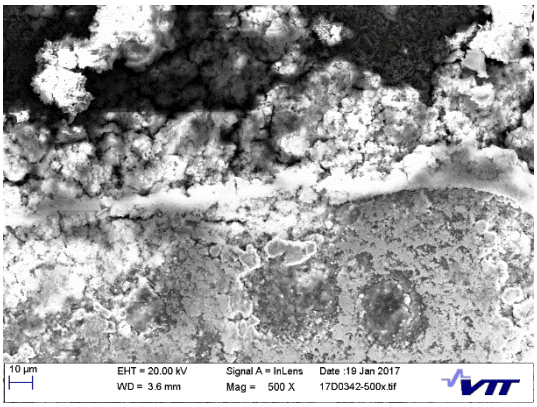

f)

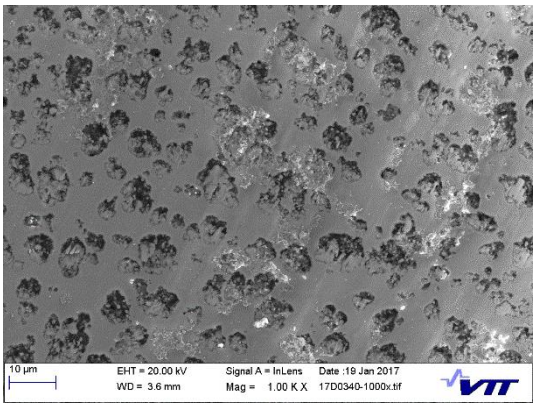

g)

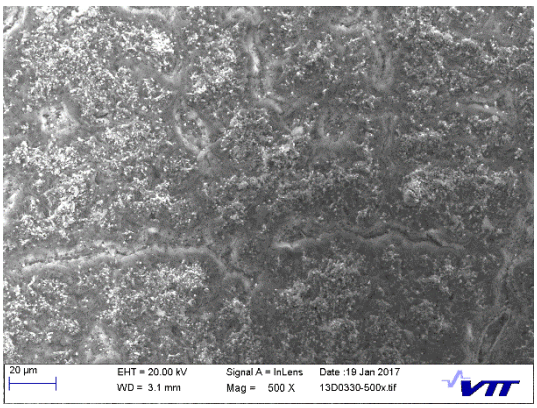

h)

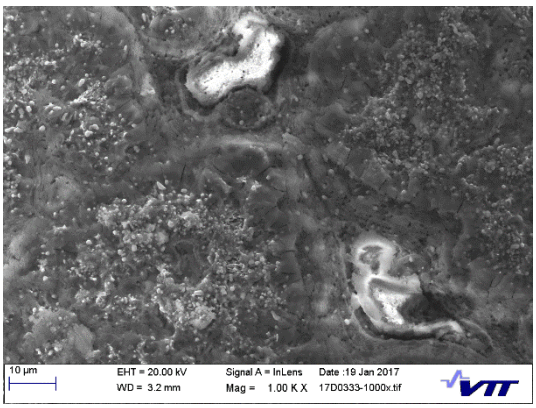

Figure 15.

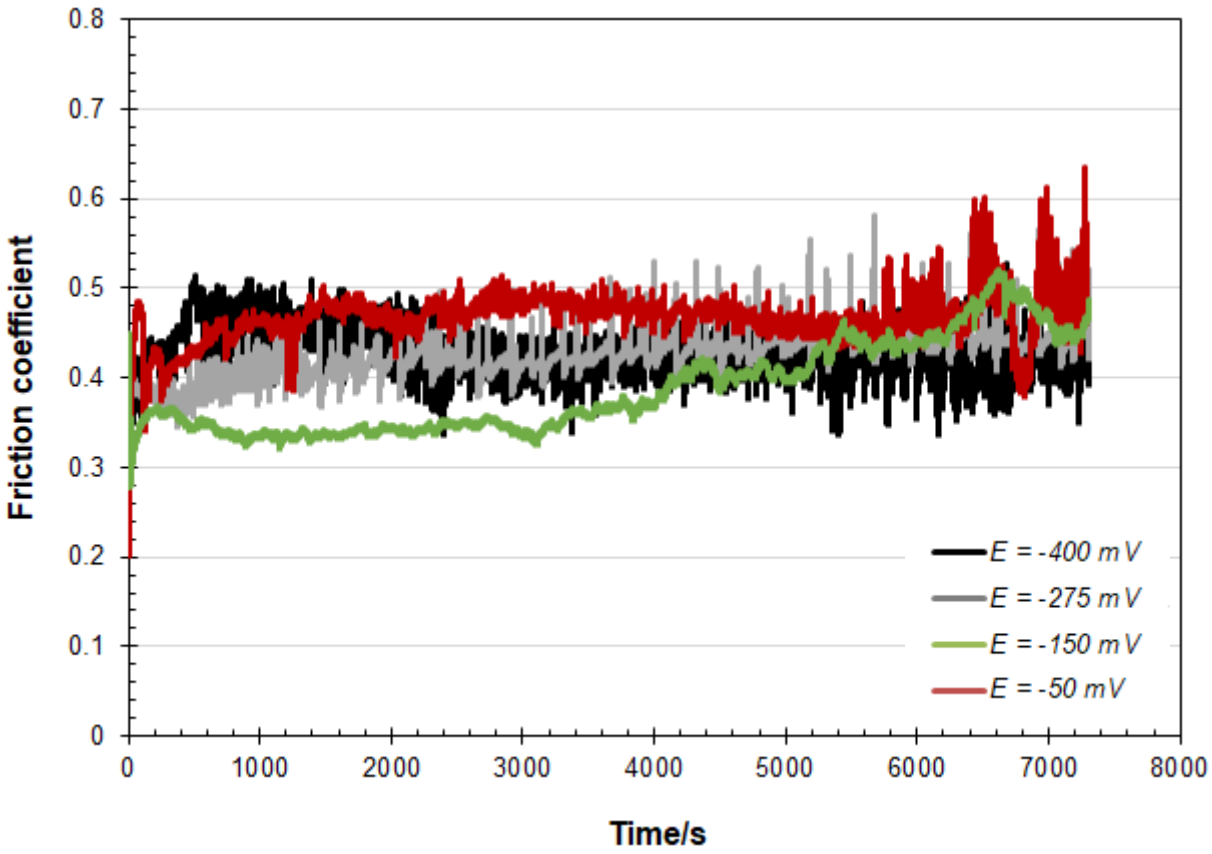
Friction coefficient
0.8
0.7
0.6
0.5
0.4
0.3
0.2
0.1
0
0
1000
2000
3000
4000
5000
6000
7000
8000
Time/s
E = -400 mV
E = -275 mV
E = -150 mV
E = -50 mV

Figure 16.

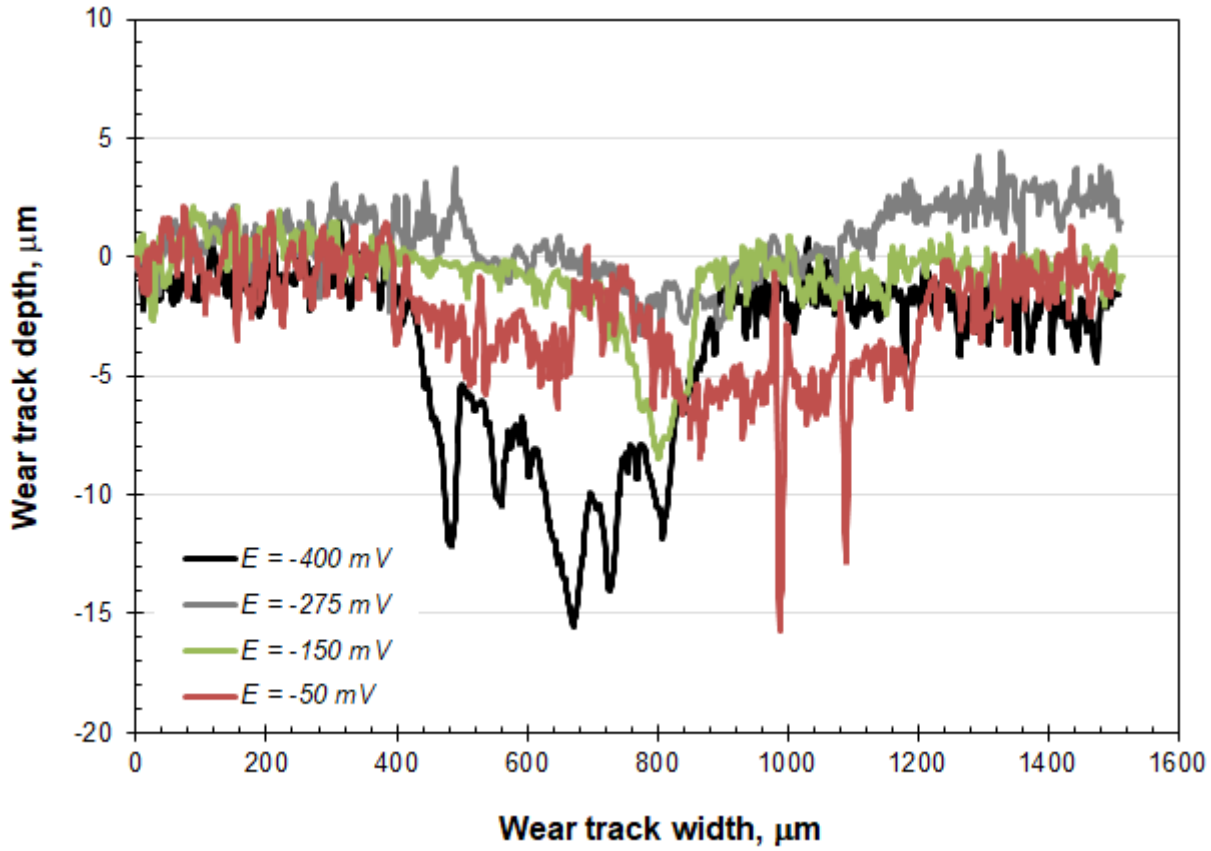
Wear track depth, µm
Wear track width, µm
E = -400 mV
E = -275 mV
E = -150 mV
E = -50 mV

a)

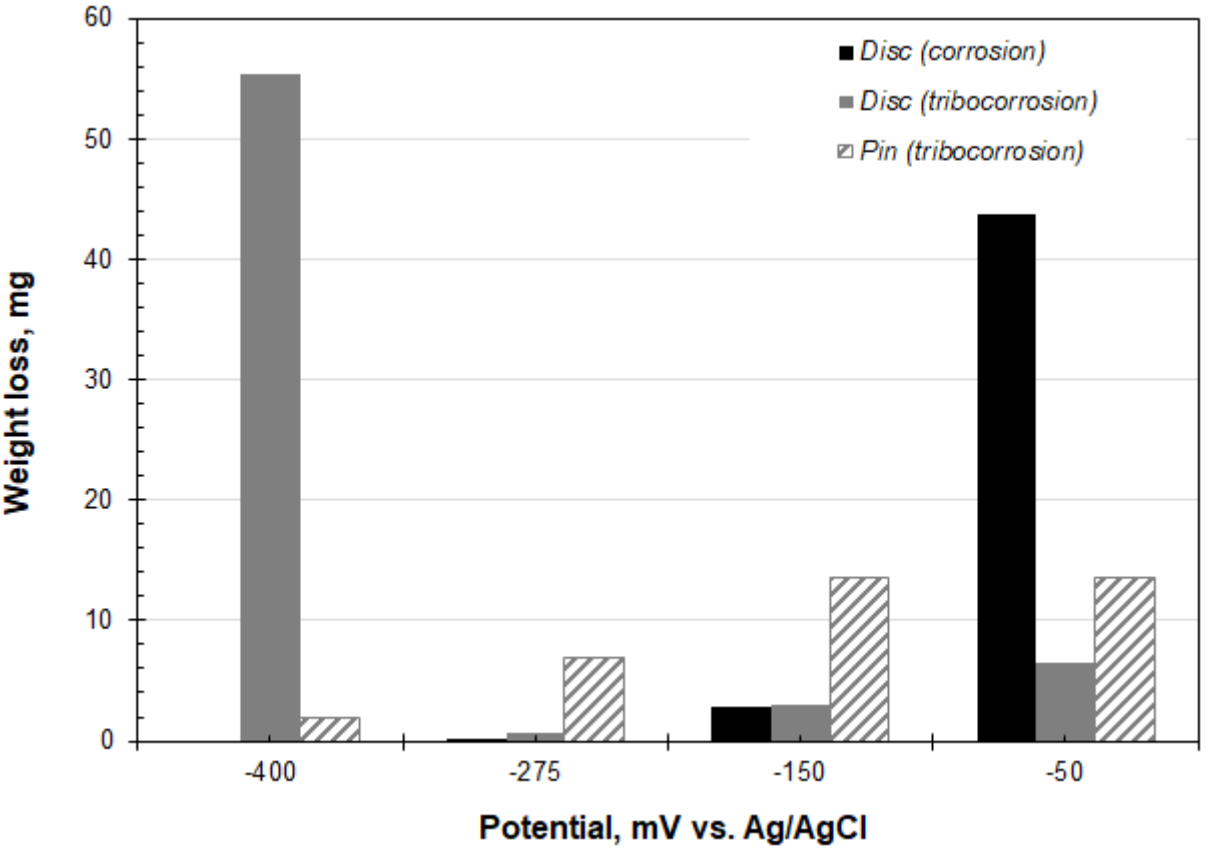
Weight loss, mg
Potential, mV vs. Ag/AgCl
Disc (corrosion)
Disc (tribocorrosion)
Pin (tribocorrosion)

b)

Figure 17.

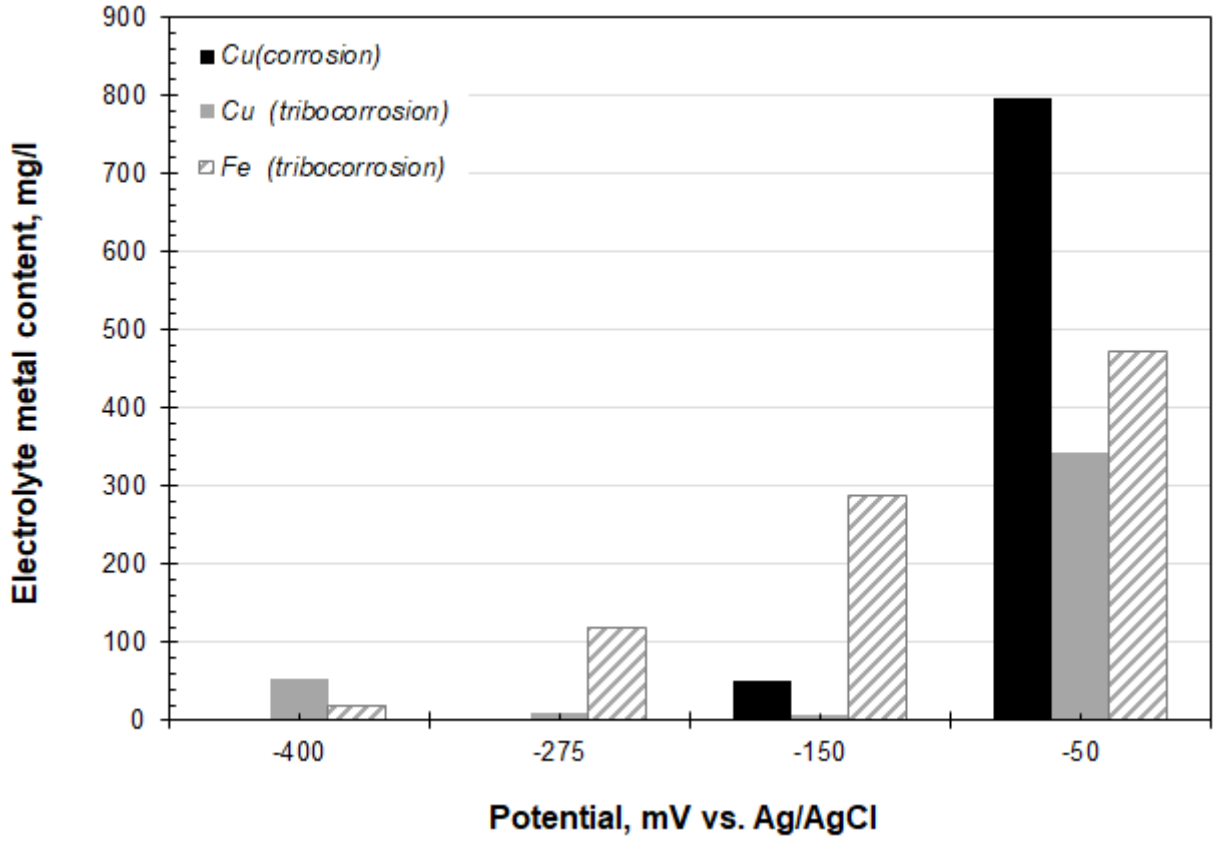
900
800
700
600
500
400
300
200
100
0
Cu(corrosion)
Cu (tribocorrosion)
Fe (tribocorrosion)
Electrolyte metal content, mg/l
-400
-275
-150
-50
Potential, mV vs. Ag/AgCl

c)

Figure 17.